

© 2012 Aaron J. King

A FREQUENCY RECONFIGURABLE SLOT ANTENNA WITH A  
CONDUCTIVE MICROFLUIDIC SWITCHING MECHANISM

BY

AARON J. KING

THESIS

Submitted in partial fulfillment of the requirements  
for the degree of Master of Science in Electrical and Computer Engineering  
in the Graduate College of the  
University of Illinois at Urbana-Champaign, 2012

Urbana, Illinois

Adviser:

Professor Jennifer T. Bernhard

# ABSTRACT

Reconfigurable antennas have the potential to provide functionality to radio systems which will make them more robust and allow for much more efficient use of the electromagnetic spectrum when combined with cognitive radio. High power applications, however, cannot benefit from the advances made in reconfigurable antenna technology in recent years due to the inability of current reconfiguration mechanisms to handle high power levels. Diodes suffer from nonlinear effects while RF MEMS have issues with self-actuation and stiction. Fluidic reconfiguration mechanisms provide an alternative to these devices which do not suffer from the same effects due to their passive behavior that is not influenced by RF signal strength. In order to investigate the suitability of fluidic conductor as a switch, a frequency reconfigurable slot antenna is designed using fluid-filled microchannels. A transmission line model is developed to provide an explanation for the behavior of the switches as well as a design procedure for the reconfigurable slot. The model is verified by building and measuring slot antennas using the microfluidic switches.

*Soli Deo gloria*

# ACKNOWLEDGMENTS

The transition to graduate school has certainly been an interesting experience, to say the least. Having spent the vast majority of my life going to class, adding the responsibility of focusing on research was quite new for me. At the same time, I had friends transitioning to a completely different lifestyle, taking full-time jobs in Massachusetts and California, Seattle and Singapore. At times, remaining in school in Champaign-Urbana made me feel left behind and stuck in the past. However, my friends in the area, both old and new, have kept me grounded, helping me look forward to my own transition out of school and reminding me that real life happens when I'm sitting in the sunshine impatiently anticipating the taste of the burger that's still browning on the grill rather than when I'm pedantically keeping track of negative signs and  $j$ 's while calculating the radiation pattern of a given current distribution.

My parents, as always, have been supportive and loving throughout my first two years in graduate school. Not only did they teach me the sense of responsibility and perseverance that I have needed to push through so far, they have continued to show their love for me with their advice and understanding.

Professor Bernhard has been extremely helpful with my transition. Not only has she taught me almost everything I know about antennas, but she has also provided me with the freedom to do work that I'm excited about, while giving me guidance, encouragement, and gentle motivational shoves when I've needed them.

I would also like to thank Jason Patrick for his work making the substrates used in this work. His excitement for the project helps fuel mine, keeping me focused on the possibilities ahead when I am wading through all of the details. Additionally, Professor Nancy Sottos and Professor Scott White have been instrumental in the development of this work.

This work has been funded by the University of Illinois ECE Distinguished Fellowship and a Department of Defense SMART scholarship.

# TABLE OF CONTENTS

CHAPTER 1	INTRODUCTION . . . . .	1
1.1	Motivation . . . . .	1
1.2	Background on Slot Antennas . . . . .	3
1.3	Background on Reconfiguration Mechanisms . . . . .	5
1.4	Thesis Outline . . . . .	11
CHAPTER 2	SLOT MODELING . . . . .	12
2.1	Introduction . . . . .	12
2.2	Transmission Line Model . . . . .	12
2.3	Antenna Feed . . . . .	19
CHAPTER 3	MICROFLUIDIC CHANNEL MODELING . . . . .	22
3.1	Introduction . . . . .	22
3.2	Transmission Line Model . . . . .	23
3.3	Slot to Microchannel Transition Model . . . . .	27
3.4	Channel Design . . . . .	30
CHAPTER 4	RESULTS . . . . .	32
4.1	Introduction . . . . .	32
4.2	Slot Results . . . . .	36
4.3	Reconfigured Slot Results . . . . .	37
4.4	Long Microchannel Slot Results . . . . .	45
4.5	Summary . . . . .	47
CHAPTER 5	CONCLUSIONS AND FUTURE WORK . . . . .	54
5.1	Conclusions . . . . .	54
5.2	Future Work . . . . .	55
REFERENCES	. . . . .	57

# CHAPTER 1

## INTRODUCTION

### 1.1 Motivation

The Federal Communications Commission (FCC) currently uses a static frequency allocation method. Frequency bands are either licensed by specific users or designated for specific purposes for various users to utilize. Separating signals in the frequency domain ensures that legal bandwidth usages will not interfere. However, this method limits the usage of the electromagnetic spectrum by only allowing a single user to ever use a given bandwidth. Allocated spectrum is not used in every location, meaning that at a given time and place there is more bandwidth available than would be indicated by the FCC's static allocation.

Consumer demands on the electronics and communications industries have been trending towards more mobile devices with access to data anywhere at any time. Laptops, netbooks, tablets, and smartphones have become far more accessible and prevalent in daily usage by the general public rather than just gadgets of interest for the electronics enthusiast. This massive increase in mobile data demand puts tremendous strain on providers to obtain and use more bandwidth to increase throughput in the network and for individual devices. The increase comes at a time when the static allocation model used by the FCC is approaching the barrier of having allocated all of the usable radio frequency (RF) spectrum, constricting the supply of mobile data at the same time that demand is growing more rapidly.

Frequency efficient solutions such as cognitive radio are currently being studied to solve this problem. Cognitive radio seeks to improve the intelligence of a radio system by allowing it to use various information to find an unused frequency band to utilize. In locations where FM radio stations or TV broadcast channels, for example, are unused, radios would be able to



use these bands for other applications instead of being restricted to sharing heavily used bands.

Reconfigurable antennas are being researched as a companion technology to cognitive radio [1]. Antenna reconfiguration has the potential to enable cognitive radio by adding functionality to a radio system. Frequency reconfigurable antennas can be built in a much smaller footprint than the frequency independent or wideband antennas which are required for cognitive radio to be able to use a variety of bandwidths without reconfiguration. Additionally, reconfigurable antennas can provide pattern or polarization reconfigurability to cognitive radio systems, allowing radios to reject interfering signals in the same frequency band as is being used. Null steering can be used to remove this interference, possibly allowing multiple users to use the same channel without interference when the location of the interferer can be determined [2].

While much of the research for reconfigurable antennas has focused on dipoles and microstrip patches, resonant slot antennas can provide much of the same functionality. Slots have not traditionally been used for many applications due to the requirement of a balun, but shrinking chip sizes allow for slot antennas to be fed by chips placed in the slot, creating a balanced feed, such as the RFID antenna designed in [3]. Additionally, the ease of adding a slot to a relatively large metal structure, creating a very low profile antenna, allows for easy implementation in numerous applications.

Currently, slot antennas are primarily used in high power radar applications. Along with military communications, radar systems also stand to benefit from the capabilities provided by reconfigurable antennas. In a similar manner to many commercial applications, military systems with the flexibility to remove interfering signals with frequency agility or spatial interference rejection will be more robust, with the added benefit of making the systems hard to detect or jam. These high power applications, however, cannot effectively use many of the reconfiguration mechanisms that are used in current research. Non-linearities and other issues that are insignificant when handling lower power signals degrade antenna performance significantly with high power levels. In order to enable the use of reconfigurable antennas in high power systems, switches must be developed which do not diminish the usefulness of the antenna by their inclusion.

Researchers are beginning to study fluidic switches as an alternative to

current active switches due to their passive, and therefore linear, behavior. This thesis explores using fluidic conductor as a switch in slot antennas to create a frequency reconfigurable antenna which does not have the same power constraints imposed by conventional switching and tuning mechanisms used in the vast majority of reconfigurable antenna research.

## 1.2 Background on Slot Antennas

Conventional slot antennas consist of a ground plane with a slot cut into it, often on a substrate with a permittivity other than that of free space. They have been in use since the 1940s, when they were used in radar [4]. Booker notes that the theory behind slots took advantage of a full electromagnetic version of Babinet's principle [4]. Slot antennas in an infinite ground plane are an exact complement to a dipole of the same length, allowing the analysis of dipoles to apply easily to that of slots. Additionally, the magnetic field polarization from a slot is parallel to the electric field polarization of its complimentary dipole, which can also be thought of as the electric fields of the two antennas having perpendicular electric field polarizations [4].

This concept can also be developed by using the surface equivalence principle developed from Maxwell's equations. The slot, assuming it is sufficiently narrow, has a constant electric field,  $\mathbf{E}$ , across the gap as shown in Figure 1.1(a). An electromagnetically equivalent problem is given when the slot is filled with conductor, to create a full infinite ground plane, with a magnetic surface current given by  $\mathbf{M}_{s1} = -\hat{\mathbf{n}} \times \mathbf{E}$  shown from above in Figure 1.1(b) and from the side in Figure 1.1(c). This infinite ground plane can be removed using image theory by placing a parallel, equal magnitude magnetic current source the same distance away from but on the opposite side of the ground plane. In this case, this image current is in the same location as the previous  $\mathbf{M}_{s1}$ , giving radiation in the half-plane generated by a magnetic current source  $\mathbf{M}_s = 2\mathbf{M}_{s1} = -2\hat{\mathbf{n}} \times \mathbf{E}$  shown in Figure 1.1(d). This narrow, linear current source radiates as a magnetic dipole, giving the same radiation pattern as an electric dipole, but with electric fields and magnetic fields switched according to their duality relationship.

Reconfigurable slot antennas have been studied in a number of forms. The simplest takes a basic slot antenna and places a PIN diode across the slot

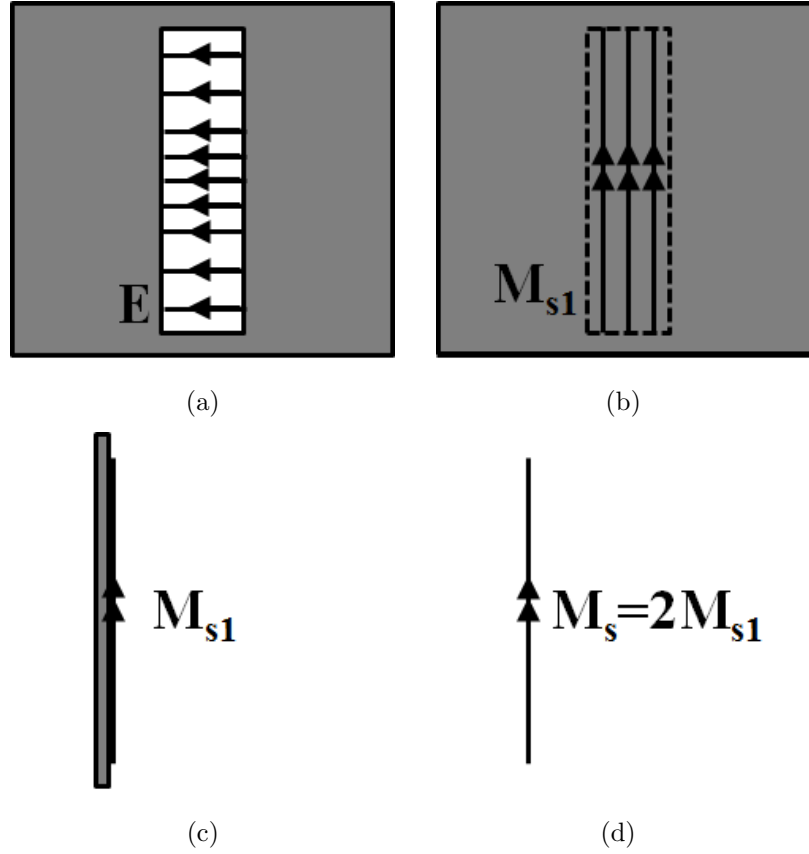


Figure 1.1: Magnetic current radiation equivalent for a slot antenna: (a) Slot top view, (b) Equivalent magnetic current top view, (c) Equivalent magnetic current side view, (d) Total magnetic current side view

to create an RF short, thereby creating a slot with a shorter physical length [5, 6]. This change in length shifts the resonant frequency of the magnetic dipole to a higher frequency, creating a frequency reconfigurable antenna. A similar method is used in [7] to effectively shorten the length of an annular slot by using RF MEMS to short out a portion of the slot length, raising the resonant frequency.

Alternatively, varactors have been used to lower the resonant frequency of slot antennas in both linear [8] and annular [9] slots. These varactors are variable capacitors which allow for continuous tuning over a frequency range. The capacitance adds phase to the current traveling along the slot, making the slot appear longer than it physically is.

The switch can be removed from the plane of the slot itself by using transmission line stubs. Chiu used a single quarter-wavelength stub with an open circuit load to attempt to short out the slot [10]. The switch actually does not change the resonance of the original slot significantly or create a resonance at the frequency that would be expected of a slot shorted at the position of the transmission line, but does create several other resonances allowing the slot to be matched at other frequencies. The reason for this issue will be discussed in Chapter 2, as this thesis uses a similar method to reconfigure a slot antenna.

Polarization reconfigurable slot antennas have been developed in several forms as well. Li created a slot antenna with switchable horizontal and vertical polarizations by using a wide slot which switches the direction of the electric field transversing the slot by redirecting current flow [11]. An annular slot antenna was also built with multiple feeds which can be selected to generate either circular or linear polarization [12]. Another annular slot antenna was designed to either switch between linear and circular polarization or left-handed circular and right-handed circular polarization by redirecting current flow around or through discontinuities in the conductor which forms the slot [13].

### 1.3 Background on Reconfiguration Mechanisms

A variety of reconfiguration mechanisms have been used for reconfigurable antennas of all types. This section will explore the various mechanisms with

their benefits and drawbacks, with emphasis on their suitability for use in high power applications.

The first issue that arises when trying to reconfigure a slot antenna is common to all of the electrical switching mechanisms: implementing a voltage bias network. Varactors, PIN diodes, and RF MEMS devices all require a voltage bias in order to tune or actuate and provide any sort of reconfigurability. A slot antenna provides a particularly difficult challenge in biasing these devices because the antenna is constructed with a continuous ground plane. This ground plane is necessary to have RF current continuity, but it also creates DC continuity across the entire antenna. Two methods have been primarily used to combat this problem, segmenting the ground plane and using an annular slot. Ground plane segmentation is enabled by using coupling capacitors to create an RF short while maintaining a DC open. This method is used in several of the aforementioned reconfigurable slot antennas, including [6] and [8]. The issue with this solution is that the RF current path is restricted to these capacitors, making the antenna performance sensitive to their placement and requiring components able to handle extremely high powers in a high power application. The annular slot is an elegant solution to this problem, used in [7] and [9], but the polarization purity that is normally available from a slot antenna is degraded significantly due to the circulating currents.

### 1.3.1 Varactors and PIN Diodes

Varactors and PIN diodes are both diode-based devices which have been designed for different uses. While varactors provide tunability to get a continuous range of operating frequencies, PIN diodes, which are generally either on or off, can still be used as discrete tuning mechanisms. However, diodes are nonlinear devices, and therefore suffer from nonlinear effects.

When a harmonic input signal given by  $S_i(t) = A \cos(\omega t)$  is affected by a nonlinear system, the resultant signal output can be represented using a Taylor series as

$$S_o(t) = \sum_{n=0}^{\infty} B_n [S_i(t)]^n = \sum_{n=0}^{\infty} B_n A^n \cos^n(\omega t). \quad (1.1)$$

The first-order term is  $B_1 A \cos(\omega t)$  while the third-order term can be rewritten as

$$B_3 A^3 \cos^3(\omega t) = \frac{3}{4} B_3 A^3 \cos(\omega t) + \frac{1}{4} B_3 A^3 \cos(3\omega t), \quad (1.2)$$

which gives a term at the same frequency as the first-order term. The third-order term has a negative coefficient  $B_3$  and a cubic dependence on the magnitude of the input signal, indicating a degradation of the output power which increases with input power. This effect, called gain compression, limits the power handling capabilities of nonlinear devices.

Similarly, two tones with radian frequencies  $\omega_1$  and  $\omega_2$  in the passband will generate third-order terms with cubic dependence on input signal magnitude that are located at  $2\omega_1 - \omega_2$  and  $2\omega_2 - \omega_1$ . These terms will be in or near the passband, distorting the signal in an effect called intermodulation distortion.

These effects will be very similar in antennas that use either varactors or PIN diodes. Sonkki and Lim have both observed intermodulation distortion effects in the antennas they designed [14, 15]. Lim specifically found that the input power which would generate third order harmonics of the same strength as first order harmonics would be 25 dBm, assuming no gain compression. White found that his antenna had a 1 dB gain compression input power of between -5 dBm and 20 dBm over his frequency range, when measuring the gain of the antenna at a fixed angle [9]. A thorough investigation of this effect was performed by Yong, who measured the full gain pattern of a tunable patch antenna at various input powers and noted that the gain compression applies to the entirety of the gain pattern equally [16]. He also found that the reciprocity relationship that is used in wireless systems does not apply with nonlinear devices, as the transmitting antenna must handle much higher power levels than the receiving antenna [16].

### 1.3.2 Radio Frequency Microelectromechanical Systems

Radio frequency microelectromechanical (RF MEMS) systems seek to provide variable capacitor or switching capabilities with conductive plates which are positioned using DC electric fields. MEMS systems require low power to remain in a given location, consuming very little while the device remains in that state. The passive behavior of conductive plates implies linear behavior,

but the RF fields will actually move the plates from their positions at a DC bias, generating nonlinear behavior [17]. Therefore, gain compression and intermodulation distortion effects will play some part in MEMS systems.

However, these effects are small in comparison to self-actuation and stiction issues. Self-actuation occurs when the bias has not actuated a switch, but high RF powers generate strong enough fields that the switch changes state. The bias voltage therefore will not have control of the switch, rendering it useless. Similarly, stiction occurs when a switch has been actuated, either by the bias voltage or self-actuation, and the high power RF signal will not allow it to release when the bias voltage is changed. Again, the bias becomes useless in controlling the switch. The maximum power where stiction does not occur tends to be lower than the power at which self-actuation occurs, making it the more problematic issue [18].

RF MEMS also tend to require high bias voltages, though work has been done to lower the requirement to more usable levels. However, in order to avoid the self-actuation and stiction problems, the DC electric field must be strong enough to overwhelm the RF electric field, keeping the required bias levels high [19] and implying that particularly high power systems will require excessively large bias voltages.

### 1.3.3 Photoconducting Switches

The electrical bias voltage problems can be overcome by using a different method to adjust the properties of the device. Panagamuwa demonstrated a dipole antenna which used photoconducting switches to reconfigure the resonant wavelength and, therefore, operating frequency of the dipole [20]. The switches have high resistivity and are actuated by using incident light to generate charge carriers to make the switch more conductive. The ground plane issue for slot antennas does not appear with this switch because the bias is optical rather than electrical, so ground plane segmentation or annular slots are unnecessary. However, the optical bias requires a constant power input while the switches are conductive, with Panagamuwa's antenna needing at least 20 mW of power to keep just two switches actuated [20]. Additionally, the silicon switches which he uses have much lower conductivity than copper, even with a large number of charge carriers, causing the antenna efficiency

to suffer, which will heat up the antenna significantly in high power systems. The problems can be reduced to a limited degree with much higher input optical powers, which will generate more charge carriers and increase conductivity, but this solution further increases the power requirement of these switches and still does not generate a conductivity near that of copper.

#### 1.3.4 Mechanical and Fluidic Reconfiguration

An alternative to using electrical or optical signals for biasing switches and varactors is to use mechanical systems. By controlling the position of the conductors in the switch mechanically rather than electrically, self-actuation and stiction problems can be avoided and nonlinear behavior will not be generated. Without these issues, these antennas can be designed to handle much higher powers. Bernhard et al. demonstrated a patch antenna with a parasitic patch which was positioned using piezoelectrics [21]. This antenna had variable frequency, gain, and bandwidth. Fluidic conductors have also been used in stretchable dipoles [22, 23] and patch antennas [24]. All four of these antennas, however, require precise mechanical positioning in order to tune to the correct frequency, which can be difficult and expensive to do. The positioning will also be significantly slower than the devices discussed previously.

Rather than precisely positioning conductors, conductive fluid flow can be used to create a fluidic reconfiguration mechanism. Khan built an antenna which had four segments of conductive fluid contained by closely spaced posts [25]. These regions could be combined by inducing fluid flow with pressure on the filled regions. The antenna resonant frequency became lower as the radiating element combined with more conductive fluid-filled regions, lengthening the element. This switch can only be activated once, as the fluidic regions cannot be separated, but conductive fluid flow was demonstrated as a useful method of antenna reconfiguration.

Alternatively, the reconfiguration mechanism can consist of fluidic dielectrics, which will effectively change the electrical size of a radiating element. A dielectric resonator antenna was demonstrated in [26] that can be filled to various heights with dielectric fluid, changing the natural resonant frequency of the cavity. A similar method would be to fill the cavity with dielectrics of



Table 1.1: Advantages and disadvantages of reconfiguration mechanisms

Switch Type	Advantages	Disadvantages
Varactors	Tunable	Nonlinear effects
	Fast tuning	Bias network
PIN Diodes	Fast switching	Nonlinear effects
		Bias network
RF MEMS	Power requirement	Self-actuation and stiction
		High voltage bias network
Photoconducting	No voltage bias	Power requirement
		Resistive loss
Mechanical	Passive	Slower
	Handles high power	Precise positioning
Fluidic	Passive	Slower
	Handles high power	Pumping mechanism

different permittivities, changing the electrical lengths of the cavity dimensions. Slots and dipoles cannot easily take advantage of these methods, as the bulk of the surrounding medium’s permittivity would have to be changed.

Because of the passive nature and lack of electrical bias network required for fluidic conductor switches, this work seeks to demonstrate a slot antenna which uses this switching method. The antenna utilizes composite fabrication technology developed in [27] to embed microchannels into the antenna substrate. The channel construction method is summarized in Section 3.1.

### 1.3.5 Summary of Reconfiguration Mechanisms

While each of these reconfiguration mechanisms is useful in certain applications, care must be taken to ensure that the correct device is used for a given application. Table 1.1 summarizes the basic advantages and disadvantages of the various devices discussed in this section. Varactors, PIN diodes, and RF MEMS devices are difficult to include in slot antennas due to their need for an electrical bias network and cannot be used in high power applications due to either nonlinear behavior or self-actuation and stiction issues. Photoconducting switches require large bias powers and have poor efficiency for RF performance. Mechanical and fluidic reconfiguration have much more promise for high power systems, but must be studied in more detail to develop useful switches.

## 1.4 Thesis Outline

This thesis will develop the design for a frequency reconfigurable slot antenna using conductive liquid switches. Chapter 2 will develop a transmission line model for the slot antenna in order to improve the design process for the antenna. Chapter 3 will develop the circuit model of the fluidic switch to be included in the slot antenna model so that the antenna can be designed for a given switched resonant frequency with predictable effects. In Chapter 4 the measured results of the antenna will be presented and evaluated while comparing with the transmission line model developed in the previous chapters. Finally, Chapter 5 will discuss the conclusions from this study and the future work required to continue the development of microfluidic switching mechanisms for antennas.

# CHAPTER 2

## SLOT MODELING

### 2.1 Introduction

Antennas are transducers between guided and unguided electromagnetic waves. Therefore, analysis needs to be performed on both the guided, or circuit, characteristics of the antenna as well as the unguided, or radiation, characteristics. A transmission line model can often be used to approximate the circuit characteristics of an antenna without performing full-wave analysis. While the radiation characteristics influence the circuit behavior of the antenna heavily, radiation models can be used to easily calculate these characteristics. The slot antenna which is studied in this work is pictured in Figure 2.1. The antenna consists of a narrow rectangular slot of length  $L_s$  and width  $W_s$  cut in a ground plane supported by a substrate of height  $d$  with permittivity  $\epsilon_r$ . The slot is fed with a coaxial cable at a point at a distance of  $C$  from one end of the slot.

### 2.2 Transmission Line Model

The transmission line model for the slot is that of a lossy transmission line as shown in Figure 2.2. The slot is fed off-center with a distance of  $C$  from one end, giving two parallel fed stubs of lengths  $C$  and  $L_s - C$ . The load at the end of each stub is a short created by the ground plane along the narrow width of the slot with respect to a wavelength. The slot has a characteristic impedance denoted by  $Z_{s0}$  along with a complex propagation constant  $\gamma_s = \alpha_s + j\beta_s$ . The lossless propagation constant  $\beta_s$  will be referred to as just the propagation constant and is determined by  $\epsilon_r$  of the substrate and is related the slotline wavelength as  $\beta_s = 2\pi/\lambda_s$ . The attenuation constant  $\alpha_s$  characterizes the

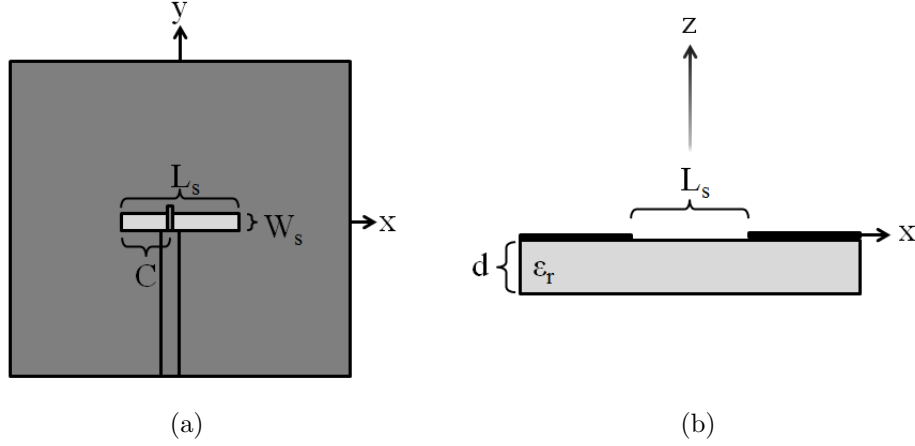


Figure 2.1: Slot antenna cross sections

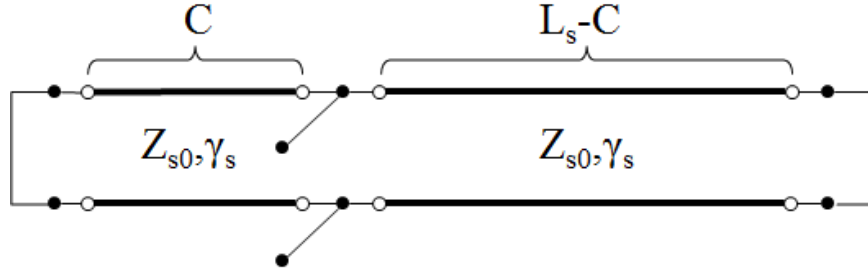


Figure 2.2: Transmission line model for the slot antenna

losses to the substrate, the conductor resistivity, and radiation. The lossless parameters will be determined by Cohn's method in the next section, while the attenuation constant will be found through conservation of energy in Section 2.2.2.

### 2.2.1 Cohn's Method

Cohn calculates the propagation constant and characteristic impedance of a slotline using a mode matching technique [28]. With fields of equal amplitude traveling in both directions on the slotline, the field magnitude is periodic with zeros located every  $\lambda_s/2$  where  $\lambda_s = 2\pi/\beta_s$ . The coordinate system can be defined as in Figure 2.3 such that two such zeros are located at  $x = 0$  and  $x = a = \lambda_s/2$ . Cohn places perfect electric conductor planes of infinite extent at these two locations, which does not disturb the fields since the transverse electric field is already zero. Next, perfect electric conducting

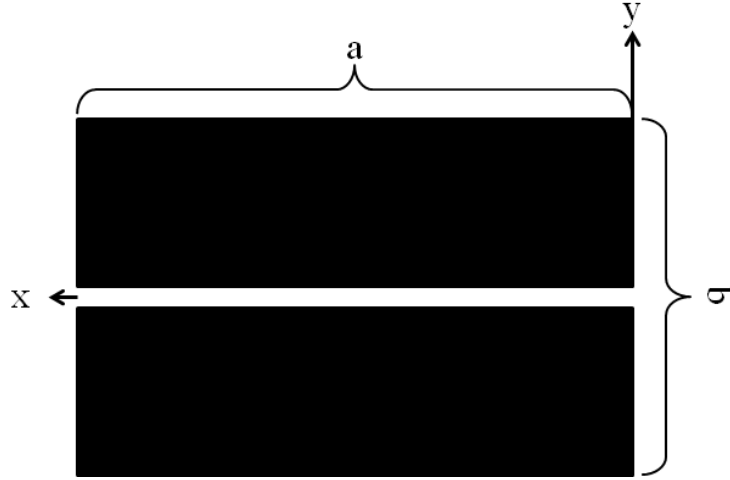


Figure 2.3: Slotline used in Cohn's method

walls are placed parallel to the slot at  $y = \pm b/2$ . These walls will affect the fields, but for  $b$  sufficiently large, the effect will be insignificant. These walls create a rectangular waveguide with the side cross section shown in Figure 2.4. The slot forms a capacitive iris in the waveguide with a dielectric slab behind it. The walls at  $\pm b/2$  can also be perfect magnetic conductors to create a different rectangular waveguide to analyze, yielding the same result when these walls are moved an infinite distance away.

The only modes which propagate along this waveguide have  $x$ -variation of  $\lambda_s/2$  due to the variation along the original slotline and field maxima in the slot, limiting the modes to just  $TE_{1,0}$ ,  $TE_{1,2n}$ , and  $TM_{1,2n}$  for  $n \geq 1$ . Because  $\lambda_s < \lambda_0$ ,  $a$  will be less than  $\lambda_0/2$ , which shows that these modes are all cut off in the air portion of the waveguide. The dielectric region allows for the  $TE_{1,0}$  mode and possibly a few higher modes to propagate. Cohn notes that mode matching can be performed by ensuring that the sum of the susceptances of each of the modes in both the  $+z$  and  $-z$  directions at the capacitive iris plane is equal to zero, the transverse resonance condition [28].

Using electric conducting walls at  $\pm b/2$ , the transverse fields in the dielectric region have a  $y$ -variation given by

$$E_y = R_0 + \sum_{n>0} R_n \cos\left(\frac{2\pi ny}{b}\right) \quad (2.1)$$

$$H_x = -y_{i,0}R_0 - \sum_{n>0} y_{i,n} \cos\left(\frac{2\pi ny}{b}\right) \quad (2.2)$$

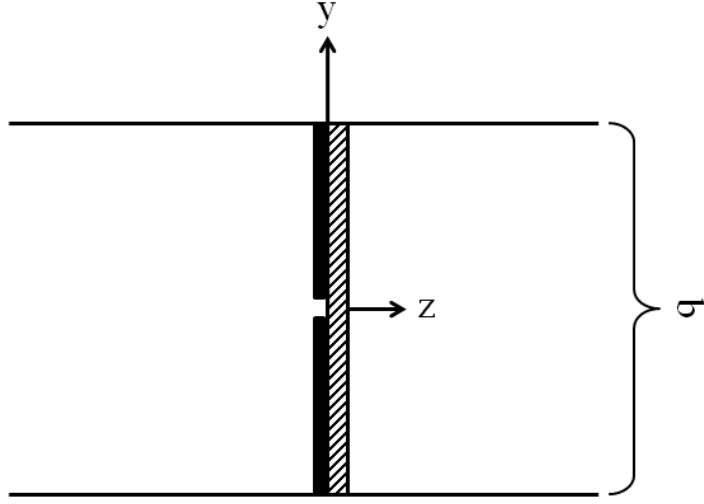


Figure 2.4: Waveguide cross section for Cohn's method

where  $R_0$  and  $R_n$  are constants and input wave admittances  $y_{i,0}$  and  $y_{i,n}$  are given by

$$y_{i,0} = - \left( \frac{H_x}{E_y} \right)_{TE_{10}} \quad (2.3)$$

$$y_{i,n} = - \frac{(H_x)_{TE_{1,2n}} + (H_x)_{TM_{1,2n}}}{(E_y)_{TE_{1,2n}} + (E_y)_{TM_{1,2n}}}. \quad (2.4)$$

A constant field distribution can be assumed in the slot for  $b \gg w_s$ , so  $b$  is chosen to be suitably large to give a field given by

$$E_y = \begin{cases} C_0, & |y| \leq w_s/2 \\ 0, & \text{else} \end{cases} \quad (2.5)$$

$$H_x = \begin{cases} y'_i C_0, & |y| \leq w_s/2 \\ 0, & \text{else} \end{cases} \quad (2.6)$$

with  $y'_i$  as the input wave admittance to the iris formed by the slot. These fields need to be equal at  $z = 0$ , allowing for a Fourier series analysis to be performed to find  $R_0$  and  $R_n$  and a relationship to be found between the input admittances to the capacitive iris and to the dielectric region given by

$$\frac{b}{w_s} y'_i = y_{i,0} + 2 \sum_{n>0} y_{i,n} \text{sinc}^2(\pi n \delta) \quad (2.7)$$

with  $\delta = b/w$ . Using  $Y_{i,n} = (a/2b)y_{i,n}$  and  $Y_i = (a/2w)y'_i$ , the guide admittances for each mode, the relationship can be expressed as

$$Y_i = Y_{i,0} + 2 \sum_{n>0} Y_{i,n} \text{sinc}^2(\pi n \delta). \quad (2.8)$$

These admittances can be found as described in the appendix of [28] for each waveguide mode, giving a solution, optimized for fast convergence, of

$$\begin{aligned} \eta B_t = & \frac{a}{2b} \left[ -v + u \tan \left( \frac{\pi du}{ap} - \tan^{-1} \frac{v}{u} \right) \right] + \frac{1}{p} \left\{ \left( \frac{\epsilon_r + 1}{2} - p^2 \right) \ln \frac{2}{\pi \delta} \right. \\ & \left. + \sum_{n>0} \frac{1}{2n} \left[ v^2 \left( 1 - \frac{1}{F_n} \right) + M_n \right] \text{sinc}^2(\pi n \delta) \right\}, \end{aligned} \quad (2.9)$$

where  $p = \lambda_0/\lambda_s$ ,  $\eta = \sqrt{\mu_0/\epsilon_0}$ ,  $u = \sqrt{\epsilon_r - p^2}$ ,  $v = \sqrt{p^2 - 1}$ ,

$$F_n = \sqrt{1 + \left( \frac{bv}{2anp} \right)^2}, \quad (2.10)$$

$$F_{n1} = \sqrt{1 - \left( \frac{bv}{2anp} \right)^2}, \quad (2.11)$$

and

$$M_n = \begin{cases} \frac{\epsilon_r \tanh r_n - p^2 F_{n1}^2 \coth q_n}{\left[ 1 + \left( \frac{b}{2an} \right)^2 \right] F_{n1}} - u^2, & F_{n1} \text{ real} \\ \frac{\epsilon_r \tan r_n - p^2 |F_{n1}|^2 \cot q_n}{\left[ 1 + \left( \frac{b}{2an} \right)^2 \right] |F_{n1}|} - u^2, & F_{n1} \text{ imaginary} \end{cases}. \quad (2.12)$$

In  $M_n$ ,  $r_n$  and  $q_n$  are given by

$$r_n = \begin{cases} \frac{2\pi nd F_{n1}}{b} + \tanh^{-1} \left( \frac{F_{n1}}{\epsilon_r F_n} \right), & F_{n1} \text{ real} \\ \frac{2\pi nd |F_{n1}|}{b} + \tan^{-1} \left( \frac{|F_{n1}|}{\epsilon_r F_n} \right), & F_{n1} \text{ imaginary} \end{cases} \quad (2.13)$$

$$q_n = \begin{cases} \frac{2\pi nd F_{n1}}{b} + \coth^{-1} \left( \frac{\epsilon_r F_n}{F_{n1}} \right), & F_{n1} \text{ real} \\ \frac{2\pi nd |F_{n1}|}{b} + \cot^{-1} \left( \frac{\epsilon_r F_n}{|F_{n1}|} \right), & F_{n1} \text{ imaginary} \end{cases}. \quad (2.14)$$

The ratio of  $p = \lambda_0/\lambda_s$ , which gives the susceptance  $B_t = 0$ , is found iteratively, giving  $\lambda_s = 2\pi/\beta_s$ . The characteristic impedance is defined to be  $Z_{s0} = V^2/2P$  with  $V$  as the peak voltage amplitude across the slot and  $P$

the average power flow of the full propagating wave. This value is given by

$$Z_0 = \eta \frac{v}{vg} \frac{\pi}{p} \frac{-\Delta p}{\Delta(\eta B_t)}, \quad (2.15)$$

where  $\eta = 120\pi$  is the impedance of free space and  $\Delta(\eta B_t)$  is given by the difference between the value of  $\eta B_t$  given in Equation 2.9 for values of  $p' = p \pm \Delta p/2$  around the solution point,  $p$ . The ratio of the phase and group velocities is given by

$$\frac{v}{v_g} = 1 + \frac{f}{p} \frac{\Delta p}{\Delta f} \quad (2.16)$$

with  $\Delta p$  and  $\Delta f$  calculated in this case for differing values of  $a = \lambda_0/2$ .

The conducting walls at  $\pm b/2$  are then moved farther from the slot until the solution converges to a point where these walls do not affect the field on the slotline. Cohn found that both the electric and magnetic conducting walls gave the same solution at convergence, allowing for either to be used [28].

### 2.2.2 Radiation and Loss in the Transmission Line Model

Cohn's method only provides the parameters of the transmission line which describe the wave propagation along the slot. The input impedance of such an antenna will be purely imaginary, yielding an input reflection coefficient with a magnitude of one because no radiation has been taken into account. The radiation from the slot at resonance can be included in the transmission line model as an attenuation constant  $\alpha_s$ , or loss per unit length [29].

The method begins by finding the electric field in the slot aperture including an attenuation constant with voltage  $V_0$  at the feed generated by a 1 volt peak-to-peak RF source with  $50 \Omega$  impedance.

$$\mathbf{E}_a = -\frac{V_0}{W_s} \frac{\sinh \gamma_s \left( \frac{L_s}{2} - |x| \right)}{\sinh \gamma_s \left( \frac{L_s}{2} \right)} \hat{\mathbf{y}}. \quad (2.17)$$

The surface equivalence principle can be used to treat this field as a radiating



magnetic surface current.

$$\mathbf{M}_s = 2\mathbf{E}_a \times \hat{\mathbf{n}} = -\frac{2V_0}{W_s} \frac{\sinh \gamma_s \left( \frac{L_s}{2} - |x| \right)}{\sinh \gamma_s \left( \frac{L_s}{2} \right)} \hat{\mathbf{x}} \quad (2.18)$$

The power radiated in the far field from this magnetic current distribution is given in [3] to be

$$P_r(\alpha_s) = \frac{\zeta |k|^2 |V_0|^2 |\gamma_s|^2}{\eta \pi^2 \left| \sinh \left( \gamma_s \frac{L_s}{2} \right) \right|^2} \int_0^\pi \int_0^{\frac{\pi}{2}} \frac{\sin^2 \phi + \cos^2 \phi \cos^2 \theta}{|\gamma_s^2 + w^2|^2} \\ * \left| \cosh \left( \gamma_s \frac{L_s}{2} \right) - \cos \left( w \frac{L_s}{2} \right) \right|^2 \sin \theta d\theta d\phi \quad (2.19)$$

with

$$\zeta = 1 + \frac{1}{\sqrt{\epsilon_r}} \quad (2.20)$$

as a weighting constant to incorporate the radiation into both the upper half-space of air and the lower half space which includes the dielectric slab. Additionally,  $w = k_0 \sin \theta \cos \phi = k_x$  and  $\eta = 120\pi$  is the impedance of free space.

The power radiated should be equal to the power lost in the transmission line model for the same voltage at the input. This power is considered to be the incident power to the model and can be calculated as

$$P_i(\alpha_s) = \frac{1}{Z_c} \frac{\tanh \left( \alpha_s \frac{L_s}{2} \right) \left[ 1 + \tan^2 \left( \beta_s \frac{L_s}{2} \right) \right]}{\left[ 2 \frac{Z_0}{Z_{s0}} + \tanh \left( \alpha_s \frac{L_s}{2} \right) \right]^2 + \tan^2 \left( \beta_s \frac{L_s}{2} \right) \left[ 1 + 2 \frac{Z_0}{Z_{s0}} \tanh \left( \alpha_s \frac{L_s}{2} \right) \right]^2} \quad (2.21)$$

While a more comprehensive model for the radiation of the slot was developed in [3], only one resonance was required for this antenna, which was found to be adequately modeled by the loss per unit length parameter.

In addition to the loss due to radiation, the substrate has significant loss as an epoxy glass. The loss tangent was approximated to be  $\tan \delta = 0.04$ , on the high end for FR-4 fiberglass. A model for this loss was developed in [3], but was implemented by including a conductance per unit length argument. In order to add this loss to the model, the parameters that have been used

up to this point must be converted to the more fundamental transmission line parameters  $\mathcal{R}$ ,  $\mathcal{L}$ ,  $\mathcal{G}$ , and  $\mathcal{C}$ , where

$$\mathcal{R} = \text{Re} \left\{ \frac{\gamma_s}{Z_{s0}} \right\} \quad (2.22)$$

$$\mathcal{L} = \text{Im} \left\{ \frac{\gamma_s}{Z_{s0}} \right\} \quad (2.23)$$

$$\mathcal{G} = \text{Re} \left\{ \frac{\gamma_s Z_{s0}}{2\pi f_0} \right\} \quad (2.24)$$

$$\mathcal{C} = \text{Im} \left\{ \frac{\gamma_s Z_{s0}}{2\pi f_0} \right\} \quad (2.25)$$

with  $f_0$  as the designed resonant frequency for the slot. The effect of the loss tangent is then included using the conductance per unit length parameter from [3] where

$$\mathcal{G}_{loss} = 2\pi f \tan \delta \epsilon_0 \epsilon_{effs} 4 \frac{h_m}{W_s}, \quad (2.26)$$

where  $f$  is the frequency of the signal,  $\epsilon_{effs}$  is the effective relative permittivity of the slot, and  $h_m$  is the metal thickness. This conductance is then added to the conductance without dielectric loss, and the resulting impedance and complex propagation constant are then given by

$$\gamma_{sl} = \sqrt{(\mathcal{R} + j2\pi f_0 \mathcal{L})(\mathcal{G} + \mathcal{G}_{loss} + j2\pi f_0 \mathcal{C})} \quad (2.27)$$

$$Z_{sl0} = \sqrt{\frac{\mathcal{R} + j2\pi f_0 \mathcal{L}}{\mathcal{G} + \mathcal{G}_{loss} + j2\pi f_0 \mathcal{C}}} \quad (2.28)$$

where  $\gamma_{sl}$  and  $Z_{sl0}$  are used in the transmission line model if loss plays a significant role in the dielectric.

## 2.3 Antenna Feed

A balun is required in order to feed the slot antenna with a coaxial line. The Dyson balun is the simplest balun to construct for a slot antenna and gives the bandwidth necessary to demonstrate a frequency reconfigurable antenna. The balun is created by soldering the center pin of the coaxial line to one side of the slot and the outer conductor to the opposite side along the entire

length of the ground plane [30]. This configuration is an effective balun as long as the currents are significantly diminished in magnitude at the point where the coaxial line is no longer soldered to the ground plane [30], which is true for a slot antenna with a ground plane which is several wavelengths in each dimension.

The input impedance of the antenna can be adjusted by moving the feed along the length of the slot. A matched input impedance can be achieved by locating the feed at the right point along the antenna. In Figure 2.1, the feed location is shown to be a distance  $C$  from the end of the slot. This placement is reflected in the transmission line model in Figure 2.2. The input impedance of the antenna is given by the parallel combination of the input impedances of the two lossy stubs with shorts as a loads,  $Z_{s1}$  and  $Z_{s2}$ :

$$Z_s = \frac{Z_{s1}Z_{s2}}{Z_{s1} + Z_{s2}} \quad (2.29)$$

The input impedances of the stubs are given by

$$Z_{s1} = Z_{s0} \tanh(\gamma_s C) \quad (2.30)$$

$$Z_{s2} = Z_{s0} \tanh(\gamma_s (L_s - C)) \quad (2.31)$$

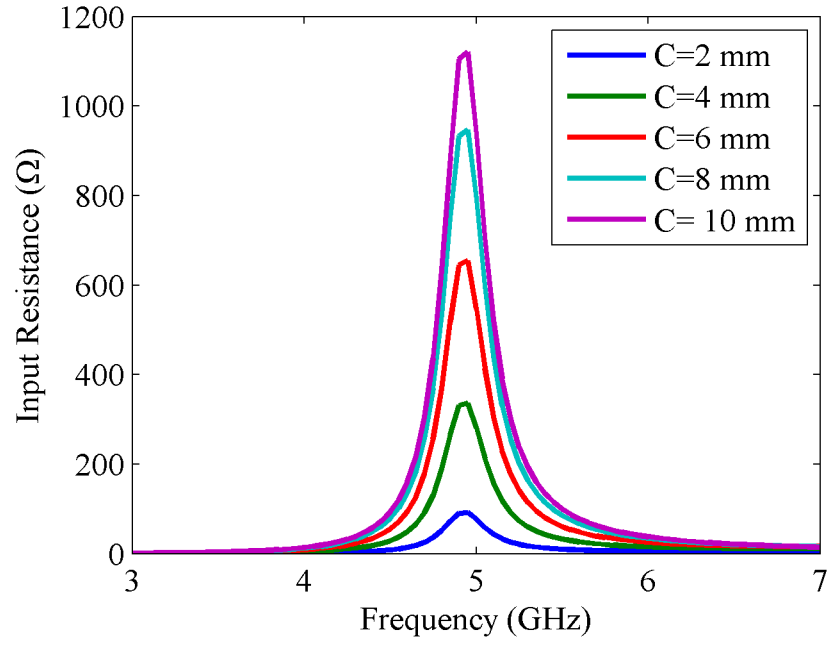
yielding

$$Z_s = Z_{s0} \frac{\tanh(\gamma_s C) \tanh(\gamma_s (L_s - C))}{\tanh(\gamma_s C) + \tanh(\gamma_s (L_s - C))}. \quad (2.32)$$

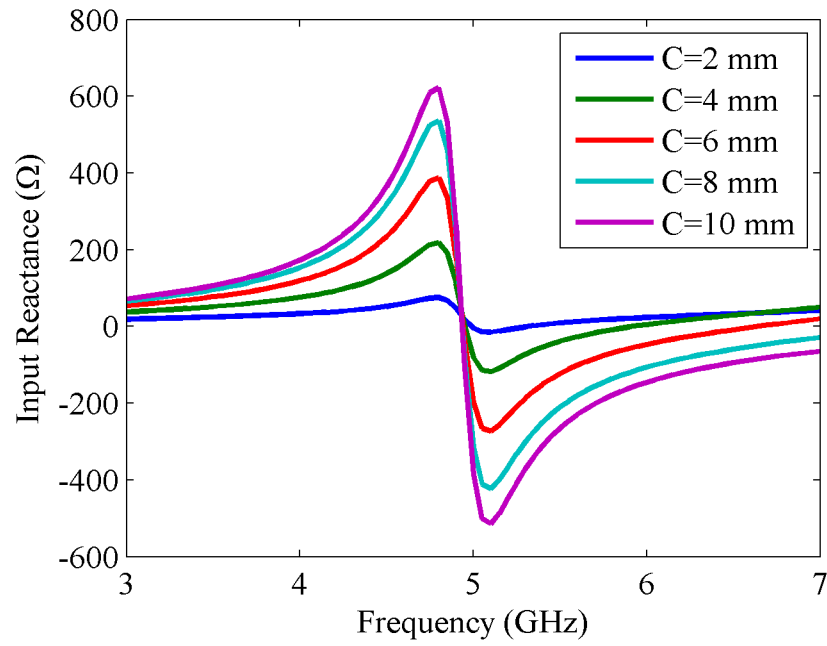
For a center-fed slot where  $C = L_s/2$ , the input impedance will be given by

$$Z_s = \frac{Z_{s0}}{2} \tanh\left(\gamma_s \frac{L_s}{2}\right). \quad (2.33)$$

The input impedance of a slot antenna with varying  $C$  values determined using this transmission line model is shown in Figure 2.5. The slot has a length and width of 22 mm and 1 mm, respectively, constructed on a dielectric slab of 4 mm in height. The resistance and reactance values are significantly greater for feed positions near the middle of the slot, with a 50  $\Omega$  match achieved at resonance just below 2 mm.



(a)



(b)

Figure 2.5: Input impedance of slot antenna fed at  $C$

# CHAPTER 3

## MICROFLUIDIC CHANNEL MODELING

### 3.1 Introduction

The Autonomous Materials Systems group at the University of Illinois at Urbana-Champaign, who have fabricated all the substrates used in this work, have developed a method to embed microchannels in fiber-reinforced composites [27]. Catalyst-impregnated polylactide (PLA) sacrificial fibers are woven into the composite fabric, as shown in Figure 3.1(a). While the figure shows the sacrificial fibers being woven in the same shape as the surrounding fibers, they can be woven into many other shapes as well. The fabric is then infused with a resin and cured to form the fiber-reinforced composite. Heating the composite to above 200 °C evaporates the PLA fibers, creating the microchannels. The microchannels can then be filled with a variety of fluids for various purposes. Figure 3.1(b) depicts the channels while they are being filled.

The microchannels embedded in the substrate can be fabricated so that they run slightly underneath the surface of the dielectric substrate. The slot is built by covering one side of the substrate with copper tape and cutting a slot in it. The geometry of the channel is shown in Figure 3.2. It runs perpendicularly to the slot so that it can create a short circuit across it. The channel has a length  $L_c$  and is a distance  $h$  below the ground plane in a substrate of permittivity  $\epsilon_r$  with a thickness  $d$ . The lack of contact with the ground plane creates a two-conductor transmission line running perpendicularly to the slot. The conductor is a gallium, indium, and tin alloy called galinstan which is liquid at room temperature and has a conductivity about an order of magnitude below that of copper, or approximately  $3.5 \times 10^6$  S/m, which is significantly higher than can be achieved in silicon. However, when the microchannel is empty, the empty space is small enough to effectively

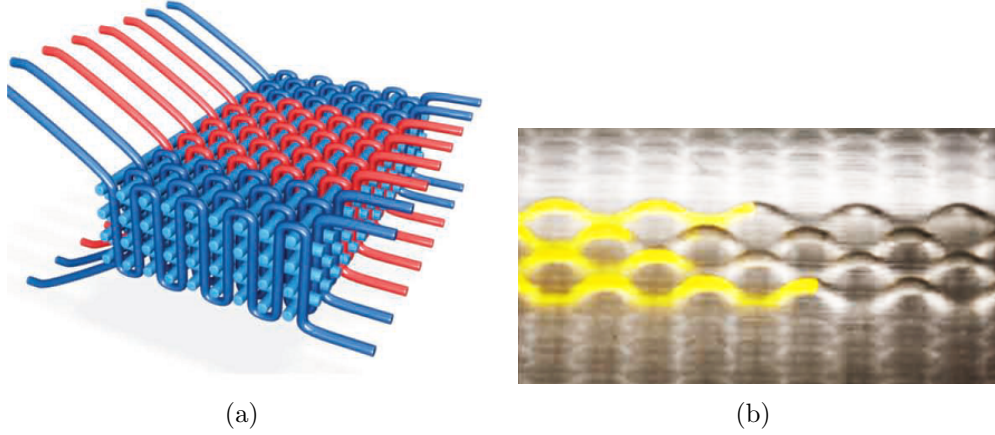


Figure 3.1: Microchannel construction: (a) Sacrificial fibers woven into the composite, (b) Microvascular channels being filled with fluid

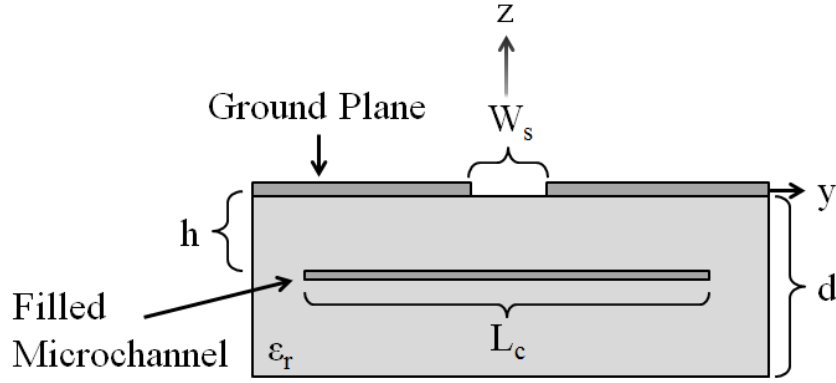


Figure 3.2: Microchannel geometry

ignore as a part of the substrate.

## 3.2 Transmission Line Model

The transmission line model of the conductor-filled microchannel is shown superimposed over the physical geometry of the channel in Figure 3.3. Two transmission line stubs with lengths  $L_c/2$  are formed, one on either side of the slot. Each stub consists of what is effectively a wire over a ground plane. The characteristic impedance and complex propagation constant are given as  $Z_{c0}$  and  $\gamma_c$ , respectively. As long as  $h \ll d$ , the fields are contained close to the ground plane, and the transmission line can be treated as if it is embedded

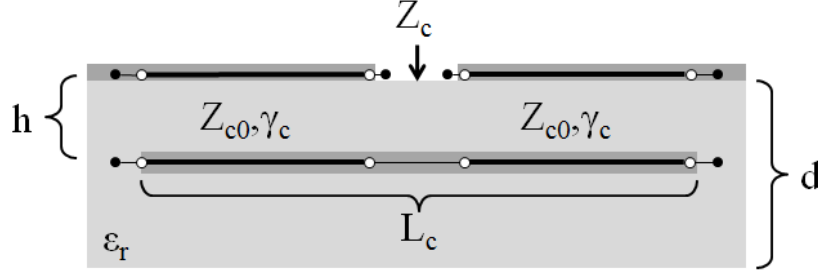


Figure 3.3: Transmission line model of the microchannel overlaid above the microchannel geometry

in an infinite medium with permittivity  $\epsilon_r$ . For the same reason, the TEM mode of the transmission line will have a guided channel wavelength of

$$\lambda_c = \frac{c}{f\sqrt{\epsilon_r}}, \quad (3.1)$$

yielding a propagation constant of  $\beta_c = 2\pi/\lambda_c$ .

The lossy transmission line model with  $\mathcal{L}$ ,  $\mathcal{C}$ ,  $\mathcal{R}$ , and  $\mathcal{G}$  can be used for this transmission line model to calculate  $\alpha_c$ . A transmission line consisting of a wire over a ground plane can be converted to a two-wire transmission line using image theory. The two-wire transmission line is well studied, with the transmission line parameters calculated as given in [31] as

$$\mathcal{L} = \frac{\mu}{\pi} \cosh^{-1} \left( \frac{2h}{D} \right) \quad (3.2)$$

$$\mathcal{C} = \frac{\pi\epsilon'}{\cosh^{-1} (2h/D)} \quad (3.3)$$

$$\mathcal{R} = \frac{2R_s}{\pi D} \quad (3.4)$$

$$\mathcal{G} = \frac{\pi\omega\epsilon''}{\cosh^{-1} (2h/D)}, \quad (3.5)$$

where  $R_s$  is the surface resistivity of the conductor, given by  $R_s = \sqrt{\omega\mu_0/2\sigma}$  and  $\epsilon' = \epsilon_r\epsilon_0$ . The dielectric loss is represented as  $\epsilon'' = \epsilon_r \tan \delta$  where  $\tan \delta$  is the loss tangent of the substrate.

This two-wire transmission line is electromagnetically equivalent to the wire over a ground plane problem because this ground plane can be replaced using image theory with a wire below the ground plane by the same distance carrying current in the opposite direction. While the fields are equivalent, the

parameters for the transmission line differ. The definition of these parameters for a general transmission line are given in [31] as

$$\mathcal{L} = \frac{\mu}{|I_0|^2} \iint_S \mathbf{H} \cdot \mathbf{H}^* ds \quad (3.6)$$

$$\mathcal{C} = \frac{\epsilon}{|V_0|^2} \iint_S \mathbf{E} \cdot \mathbf{E}^* ds \quad (3.7)$$

$$\mathcal{R} = \frac{R_s}{|I_0|^2} \int_{C_1+C_2} \mathbf{H} \cdot \mathbf{H}^* dl \quad (3.8)$$

$$\mathcal{G} = \frac{\omega\epsilon''}{|V_0|^2} \iint_S \mathbf{E} \cdot \mathbf{E}^* ds \quad (3.9)$$

where  $I_0$  is the current on the line,  $V_0$  is the voltage across the two conductors,  $S$  is the cross-sectional surface of the line, and  $C_1$  and  $C_2$  are the edges of the two conductors in that cross section. The domain of the surface integrals are half of the domain size for the wire over a ground plane as in the two-wire case because integration is performed on the same fields over only the upper half-space, halving all of the surface integrals. Similarly, the line integral is only applied to the surface of the wire with a perfect ground plane, halving the line integral, a close approximation due to the higher conductivity of the copper ground plane compared to the galinstan. Additionally, the voltage across the transmission line is a line integral from one conductor to the other, which is half of the length for a wire over a ground plane as for the two-wire case, quadrupling  $\mathcal{C}$  and  $\mathcal{G}$ . The net result of all these adjustments is that the inductance per unit length and resistance per unit length are halved while the capacitance per unit length and conductance per unit length are doubled to yield the transmission line parameters for a wire over a ground plane given by

$$\mathcal{L} = \frac{\mu}{2\pi} \cosh^{-1} \left( \frac{2h}{D} \right) \quad (3.10)$$

$$\mathcal{C} = \frac{2\pi\epsilon'}{\cosh^{-1}(2h/D)} \quad (3.11)$$

$$\mathcal{R} = \frac{R_s}{\pi D} \quad (3.12)$$

$$\mathcal{G} = \frac{2\pi\omega\epsilon''}{\cosh^{-1}(2h/D)}. \quad (3.13)$$



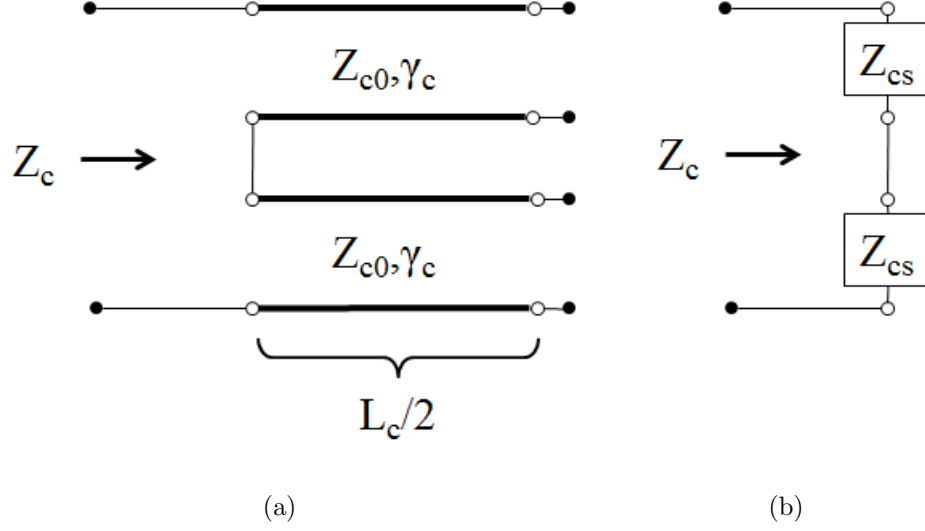


Figure 3.4: Circuit diagram for the microchannel stubs

These parameters can be used to calculate the parameters for the channel transmission line with the typical definitions

$$Z_{c0} = \sqrt{\frac{\mathcal{R} + j\omega\mathcal{L}}{\mathcal{G} + j\omega\mathcal{C}}} \quad (3.14)$$

$$\gamma_c = \alpha_c + j\beta_c = \sqrt{(\mathcal{R} + j\omega\mathcal{L})(\mathcal{G} + j\omega\mathcal{C})}, \quad (3.15)$$

though  $\beta_c$  can be approximated for a lossless case as

$$\beta_c \approx 2\pi f \sqrt{\mathcal{L}\mathcal{C}} = \frac{2\pi f \sqrt{\epsilon_r}}{c}. \quad (3.16)$$

Notably, the two transmission line stubs created by the channel shown in Figure 3.3 are connected in series. This fact can be more easily observed by redrawing the model as in Figure 3.4(a) to obtain a circuit which consists of two stubs with input impedance  $Z_{cs}$  combined in series, as shown in Figure 3.4(b). The overall input impedance of these stubs will therefore be given by

$$Z_c = 2Z_{cs} = 2Z_{c0} \coth\left(\gamma_c \frac{L_c}{2}\right). \quad (3.17)$$

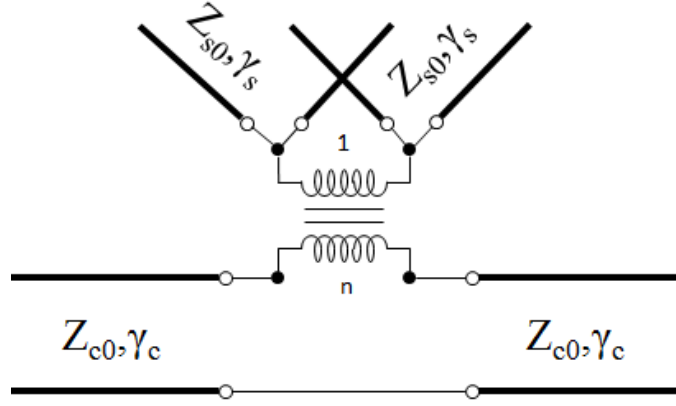


Figure 3.5: Slot to microchannel transition model

### 3.3 Slot to Microchannel Transition Model

In general the waves traveling along the slot will not necessarily transition to the microchannel cleanly, as the field distribution of each transmission line is not the same. Several methods exist to model this effect in microstrip-slotline transitions, which generally rely on an ideal transformer to transform the input impedance of the microchannel to an apparent input impedance to represent the field transition. The transformer is inserted as shown in Figure 3.5.

The first model was demonstrated by Knorr for a slotline fed by a microstrip which runs perpendicularly to it. The microchannel is approximated as a microstrip with a width equal to the microchannel's diameter  $D$ . The parameters included in this model include the vertical distance between the microchannel and the slot at their intersection  $h$ , the permittivity of the dielectric  $\epsilon_r$ , the effective wavelength on the microchannel  $\lambda_c$  and the effective wavelength in the slot  $\lambda_s$ . The turn ratio of the transformer is given in [32] by

$$n = \cos\left(2\pi \frac{h}{\lambda_c} u\right) - \cot(q'_0) \sin\left(2\pi \frac{h}{\lambda_c} u\right) \quad (3.18)$$

$$q'_0 = 2\pi \frac{h}{\lambda_c} u + \tan^{-1} \frac{u}{v} \quad (3.19)$$

where

$$u = \sqrt{\epsilon_r - \left(\frac{\lambda_c}{\lambda_s}\right)^2} \quad (3.20)$$

$$v = \sqrt{\left(\frac{\lambda_c}{\lambda_s}\right)^2 - 1}. \quad (3.21)$$

A more recent model for a transition between a microstrip and a slot was developed in [33]. This model uses reciprocity analysis to calculate the turn ratio for a given wavelength given by

$$n = \frac{J_0\left(k_{es}\frac{W_m}{2}\right) J_0\left(k_{em}\frac{W_s}{2}\right)}{k_{es}^2 + k_{em}^2} \left[ \frac{k_{em}^2 k_2 \epsilon_r}{k_2 \epsilon_r \cos(k_1 h) - k_1 \sin(k_1 h)} + \frac{k_{es}^2 k_1}{k_1 \cos(k_1 h) + k_2 \sin(k_1 h)} \right], \quad (3.22)$$

where  $J_0(x)$  is the zeroth order Bessel function of the first kind. The other parameters are given by  $k_1 = k_0 \sqrt{|\epsilon_r - \epsilon_{effs} - \epsilon_{effm}|}$ ,  $k_2 = k_0 \sqrt{|\epsilon_{effs} + \epsilon_{effm} - 1|}$ ,  $k_{es} = k_0 \sqrt{\epsilon_{effs}}$ , and  $k_{em} = k_0 \sqrt{\epsilon_{effm}}$ . The effective permittivity of the microchannel,  $\epsilon_{effm}$  is going to be the same as the substrate permittivity  $\epsilon_r$ , since the microchannel is fully embedded within the substrate. The effective permittivity of the slot  $\epsilon_{effs}$  is going to be the average of the substrate permittivity and the air,  $\epsilon_{effs} = (\epsilon_r + 1)/2$ . The other parameters required for this model are the width of the slot,  $W_s$ , and the width of the microchannel,  $W_m$ , given by its diameter,  $D$ .

Figure 3.6 shows the turns ratio required at each frequency for the slot antenna geometry which is used in this work and will be discussed more thoroughly in Chapter 4. The parameters used from this geometry include a permittivity  $\epsilon_r = 3.37$  and slot effective permittivity  $\epsilon_{effs} = 2.19$  with the channel located at  $500 \mu\text{m}$  from the ground plane. The width of the microchannel is  $500 \mu\text{m}$  while the slot has a  $1 \text{ mm}$  width. The turns ratio is almost exactly one for this geometry over the frequency band of interest, which allows the transformer to be removed while working with a slot-to-microchannel transition with these dimensions.

In order to determine how much the geometry needs to be changed to obtain a turns ratio which makes the transformer significant, the distance between the microchannel and ground plane containing the slot was ad-

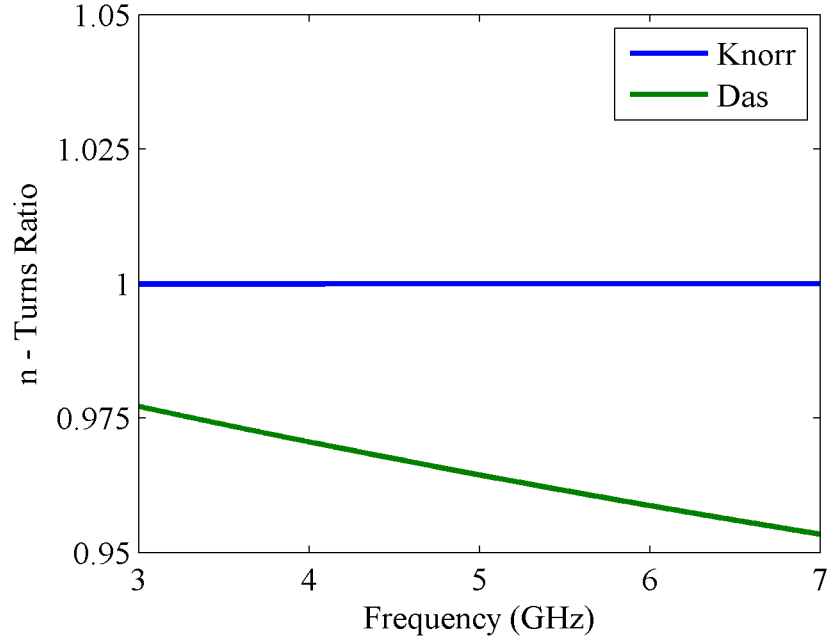


Figure 3.6: Turns ratios given by Knorr and Das

justed by 1000  $\mu\text{m}$  increments and the results using the model generated by Das in [33] were calculated. The results are shown in Figure 3.7, indicating that above approximately 2500  $\mu\text{m}$ , the turns ratio begins to increase significantly for the higher frequencies in the band of interest. At 7 GHz, this length corresponds to approximately 10% of the wavelength in the substrate, indicating that the transition has a significant effect for microchannels which are a significant part of a wavelength from the ground plane containing the slot.

The analysis of the wave transition between slot and microchannel indicates that this transition does not require special treatment for the designed antenna, and will therefore be ignored in the remainder of the analysis. However, antennas which do not have a similar geometry cannot lightly ignore this transition and must model the effects generated by the slot mode being converted to the modes propagated by the microchannel.

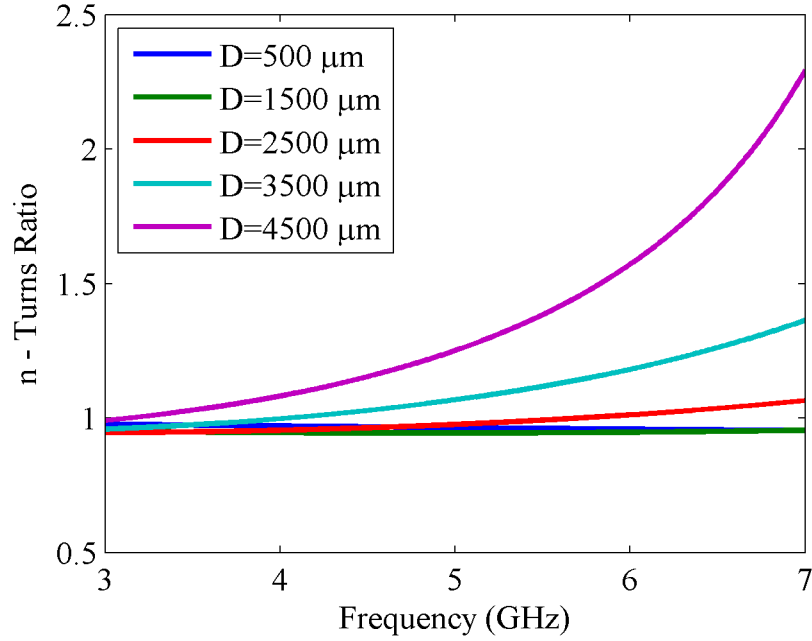
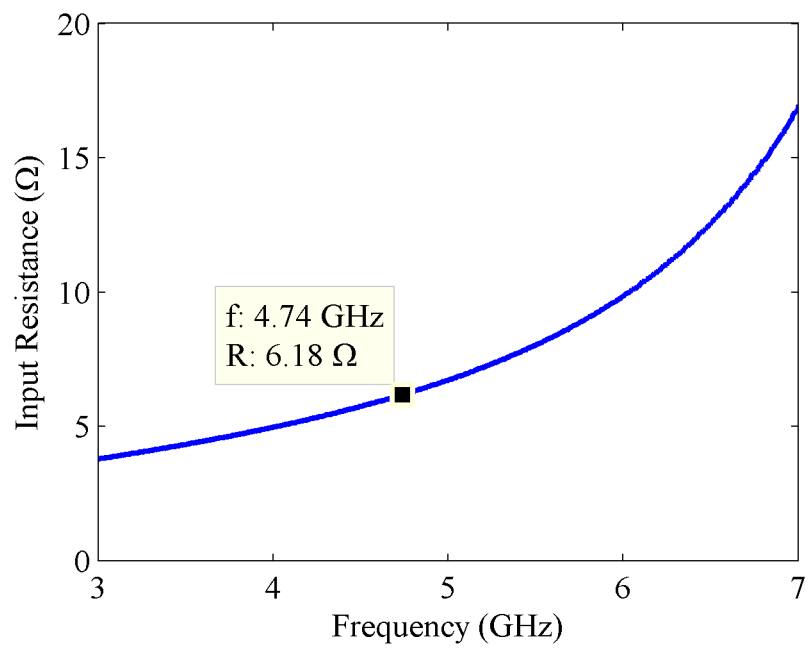


Figure 3.7: Turns ratios with varied distances of the microchannel from the ground plane given by the Das analysis

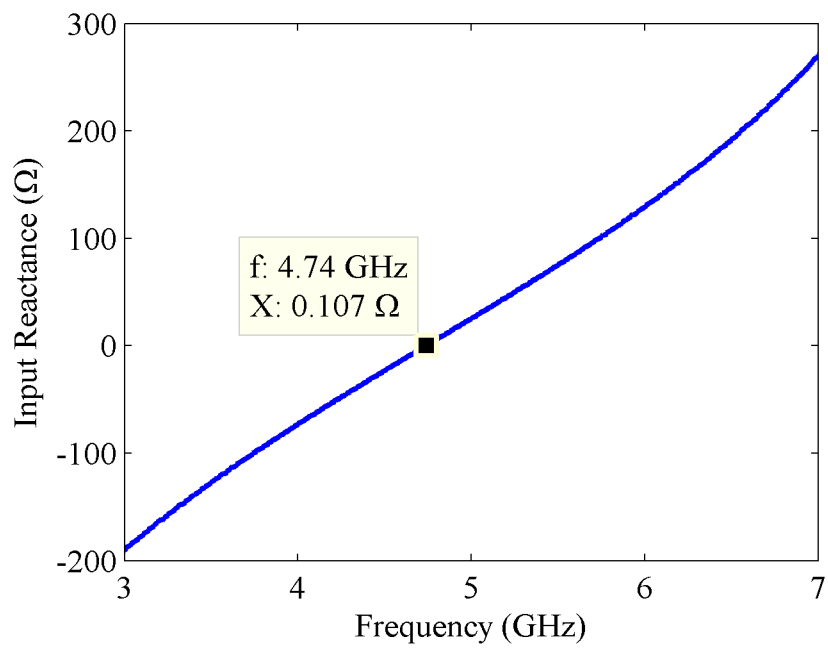
### 3.4 Channel Design

The ultimate goal of the microchannel is to design a switch that can convert an open circuit across the slot into a short circuit. Because the microchannel will not be lossless, the input impedance given by Equation 3.17 cannot give a perfect short. However, a lossless transmission line with an open circuit load will have a short circuit at the input when the length is  $\lambda/4$ . Therefore, the input impedance of a channel will be approximately a short near this frequency. For a 17 mm long channel in a substrate with permittivity of 3.37 - the values used in this thesis and discussed in depth in Chapter 4 - the input impedance is given in Figure 3.8. The first resonant frequency of this transmission line occurs where the reactance is zero, or near 4.74 GHz. The input resistance is relatively small at this resonance, so at the resonant frequency, the channel appears to be nearly a short circuit.

In order for the slot to resonate when this channel is filled, the location of the channel needs to be such that the length of the slot between the channel and opposite end is  $\lambda_s/2$ . Therefore, the location of the channel needs to be chosen along with the length of the channel so that the channel has a resonance at the same frequency that the shortened slot will resonate.



(a)



(b)

Figure 3.8: Input impedance of microchannel

# CHAPTER 4

## RESULTS

### 4.1 Introduction

The previous chapters provide a framework to design a frequency reconfigurable slot antenna using microfluidic switches. The reconfiguration mechanism operates by shorting out the slot at a given location in order to shorten the length of the slot and raise the resonant frequency of the antenna. Because the antenna is intended to be frequency reconfigurable, its radiation characteristics should not be significantly disturbed by the microchannel switch.

Figure 4.1 depicts the geometry of the antenna design, along with the various parameters which must be chosen for the antenna. The primary parameters in designing the radiating slot are the length of the slot  $L_s$ , the substrate permittivity  $\epsilon_r$ , the width of the slot  $W_s$ , and the distance of the feed from the end of the slot  $C$ . The first two parameters determine the resonant frequency of the antenna by determining the electrical length of the radiating slot, since the slot will be a half wavelength long at the resonant frequency. The effective permittivity of the slot can be approximated by averaging that of air and the substrate. The next two parameters determine the impedance match of the antenna, with  $C$  as the primary influence.

The reconfiguration of the antenna is determined by the microchannel location  $\ell$  and the microchannel length  $L_c$ . The location needs to be chosen to shorten the length of the slot to a half-wavelength at the desired resonant frequency. The microchannel needs to appear as a short circuit at this frequency, so it needs to be approximately a half-wavelength in electrical length as well. The propagation along the microchannel occurs almost entirely in the substrate, so the electrical length is determined almost solely by the substrate permittivity, so the medium is approximated as an infinite half-space

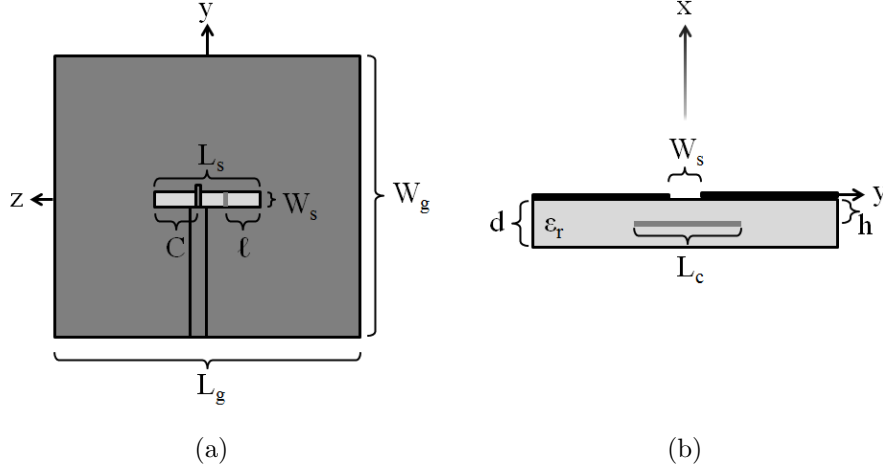


Figure 4.1: Dimensions of the frequency reconfigurable slot antenna

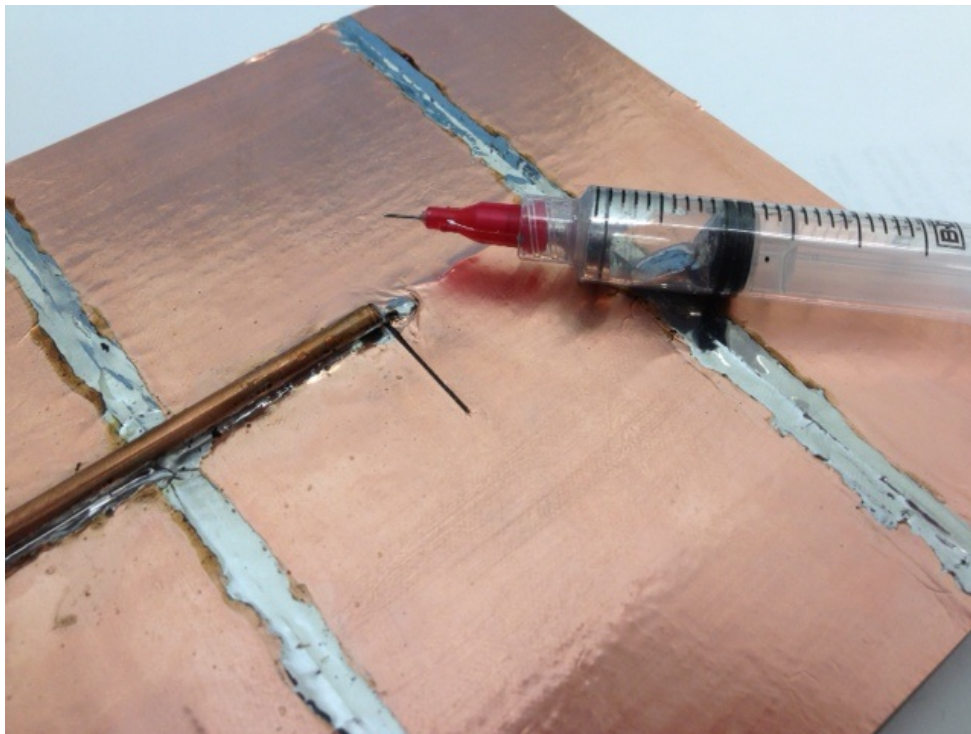
with relative permittivity  $\epsilon_r$ .

The remaining parameters are the substrate height  $d$ , the microchannel diameter  $D$ , the microchannel depth  $h$ , and the ground plane length and width  $L_g$  and  $W_g$ . The substrate height slightly affects the slot wavelength and characteristic impedance as discussed in Section 2.2.1. The microchannel diameter depth and height affect the characteristic impedance of the microchannel switch, and the ground plane dimensions will only affect radiation characteristics if the ground plane is sufficiently large compared to the slot.

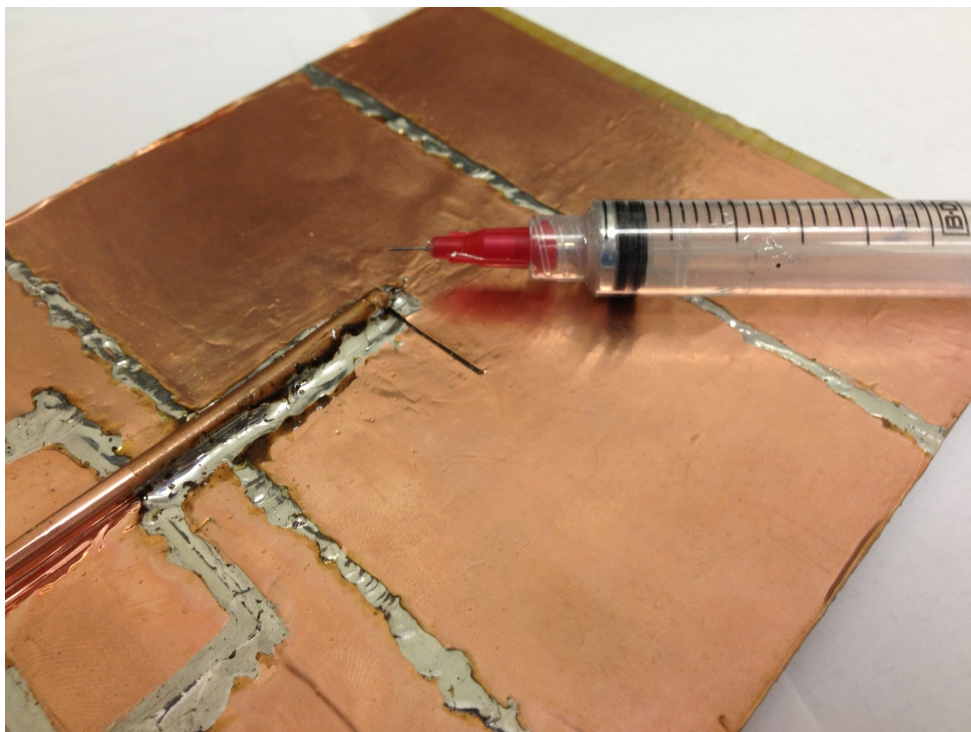
Two antennas were constructed and measured in this work. Photographs of the antennas appear in Figure 4.2, and their parameters are given in Table 4.1. The resonant frequency was chosen arbitrarily, so while the effective permittivity was determined by the substrate provided for fabrication, the slot length was chosen so that the dimensions of the antenna would be large enough to fabricate accurately by hand but small enough to avoid having an unwieldy size of ground plane without introducing significant issues generated by the finite ground plane. The slot length was chosen to be the same for each antenna, but a different resin was used for each substrate, yielding a different substrate permittivity and different slot length.

The width of the slot was chosen to be less than 5% of the slot length, or less than 2.5% of the effective wavelength along the slot, making the slot width sufficiently thin to approximate it as a magnetic dipole. With these parameters, along with the 4 mm substrate thickness  $d$ , the input impedance





(a)



(b)

Figure 4.2: Photographs of (a) Antenna 1 and (b) Antenna 2

Table 4.1: Parameters of the measured slot antennas

Parameter	Antenna 1	Antenna 2
$L_s$	21.5 mm	22 mm
$\epsilon_r$	3.37	2.95
$W_s$	0.8 mm	1 mm
$C$	1.5 mm	2 mm
$\ell_1$	4 mm	2 mm
$L_{c1}$	17 mm	140 mm
$\ell_2$	-	6 mm
$L_{c2}$	-	140 mm
$h$	500 $\mu\text{m}$	500 $\mu\text{m}$
$D$	500 $\mu\text{m}$	500 $\mu\text{m}$
$d$	4 mm	4 mm
$L_g$	140 mm	120 mm
$W_g$	140 mm	140 mm

of the slot could be designed to be  $50 \Omega$  by using Equation 2.33, calculated for various  $C$  values in Figure 2.5. Putting the coaxial feed about 2 mm from the end of the slot yields a match at resonance.

The major difference between the two antennas was the microchannels used in each. The first antenna had a single microchannel located 4 mm from the opposite edge of the slot as the feed. This microchannel was designed to be 15 mm long so that it would be  $\lambda_c/2$  at the same frequency where the slot length minus the channel location, 18 mm, is  $\lambda_s/2$ . Fabrication tolerances yielded a 17 mm long channel, with an input impedance already modeled in Figure 3.8, with a resonance at 4.74 GHz.

The second antenna was designed with channels along the entire width of the ground plane in order to validate the transmission line model. The first channel intersects the slot at  $\ell_1 = 2$  mm, giving an effective slot length of 20 mm. The frequency at which this slot length is  $\lambda_{s1}/2$  is 5.33 GHz, yielding a channel electrical length of  $4.27\lambda_{c1}$ . The second channel intersects the slot at  $\ell_2 = 6$  mm, with an effective slot length of 16 mm and a  $\lambda_{s2}/2$  frequency of 5.92 GHz. The second channel's electrical length at this frequency is  $4.74\lambda_{c2}$ .

The remaining microchannel parameters were chosen for practical purposes. The channel depth below the ground plane,  $h$  was chosen to be small to reduce radiation from the microchannel and the channel diameter was the largest available diameter for fibers used in the microchannel construction, so that the channel can carry more current. The current in the conductive

fluid will flow primarily through the cross-sectional area of the microchannel which is less than a skin depth from the surface of the conductor. The skin depth is given in [31] to be

$$\delta_s = \sqrt{\frac{2}{\omega\mu\sigma}}. \quad (4.1)$$

With a given current magnitude, the current density will be inversely proportional to the area where current flows:

$$A = 2\pi\delta_s (r - \delta_s/2), \quad (4.2)$$

where  $r = D/2$  is the channel radius and assuming that  $r > \delta_s$ . This area increases linearly with the radius of the microchannel, providing approximately a  $D^{-1}$  dependence of the current density to the channel diameter for  $r \gg \delta_s$ . At around 4.5 GHz and with a conductivity of  $3.5 \times 10^6$  S/m, the skin depth is on the order of 4  $\mu\text{m}$ . With a channel diameter of 500  $\mu\text{m}$ , this approximation holds for the microchannel in this work. The current density can be reduced with a large diameter, providing greater current capacity in the channel.

The ground plane dimensions are chosen to be about  $2.1\lambda_0$  at the lowest operating frequency, when the channels are empty, to avoid having resonances generated by lengths which are integer multiples of a half wavelength. This length is long enough to suppress some of the finite ground plane effects, though edges will still radiate to some extent.

## 4.2 Slot Results

The first slot antenna was modeled using the transmission line model from Chapter 2. Additionally, the antenna was modeled using commercially available finite element software, HFSS [34]. These results are compared in Figure 4.3 with the measured input impedance of the slot antenna. The transmission line model gives a close match in the behavior of the antenna, with the impedance magnitude matching quite well, and the resonant frequency shifted up by 0.2 GHz, or 4% of the measured resonant frequency at 4.5 GHz. This model allows for a first design pass to be made quickly and easily, with

full-wave simulations such as HFSS being used only to fine-tune the antenna design. The HFSS solution matches the measurement even more closely, with a -2% shift in frequency from the measurement, with resonance occurring at 4.4 GHz, likely caused by the lumped feed model used in the simulation.

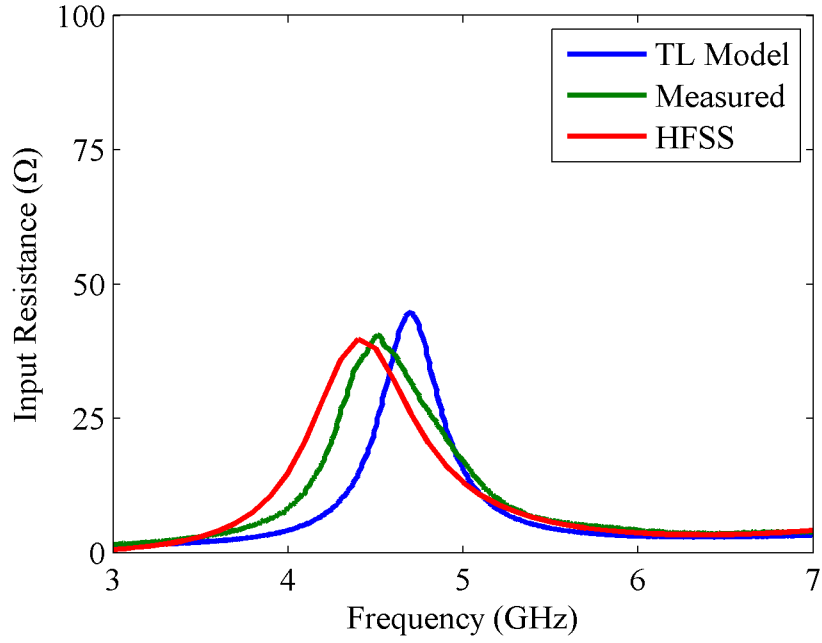
To get a better idea of the quality of the impedance match of the antenna, the VSWR of the antenna is plotted in Figure 4.4 for a 50  $\Omega$  system. The shifts in frequency reflect the same shifts found in the impedance plots. The transmission line model gives a narrower bandwidth than the other two, likely due to the fact that transmission lines only deal with a single propagation mode. The model, simulation, and measured data each indicates an impedance match, though the HFSS simulation does not quite get below the VSWR=2 limit. The measured antenna, however is well matched at the resonance frequency.

The normalized radiation patterns of the slot antenna are shown in Figure 4.5. The patterns are taken at 4.6 GHz, the frequency where the antenna has the best match. The E-plane pattern is the pattern in the xy-plane according to Figure 4.1, which should be an omnidirectional pattern for a magnetic dipole. The lobed behavior comes from the edge radiation from the finite ground plane. The edges act like elements of an antenna array which create lobes in the far field. The lobes can be diminished by using a larger ground plane, allowing currents to attenuate before reaching the edges and radiating. The H-plane patterns are taken in the xz-plane and should be the familiar dipole shaped pattern. The lobes on the top and bottom are also generated by the edge radiation of the ground plane. The co-pol direction is such that the electric field is perpendicular to the length of the slot, which is the direction of magnetic current flow in the radiation model, while the x-pol is the field polarized in the perpendicular direction.

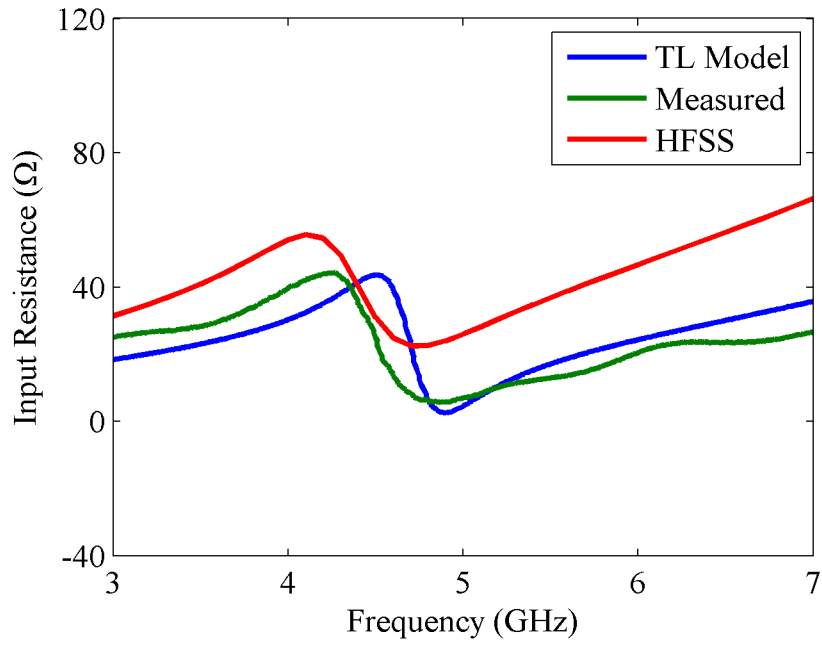
### 4.3 Reconfigured Slot Results

The first antenna is reconfigured by filling the  $\lambda_c/2$  channel with galinstan. With a perfectly constructed antenna, the new resonant frequency should be given by

$$f_1 = f_0 \frac{21.5 \text{ mm}}{17.5 \text{ mm}} = 5.5 \text{ GHz} \quad (4.3)$$



(a)



(b)

Figure 4.3: Input impedance of the slot antenna with the microchannel empty

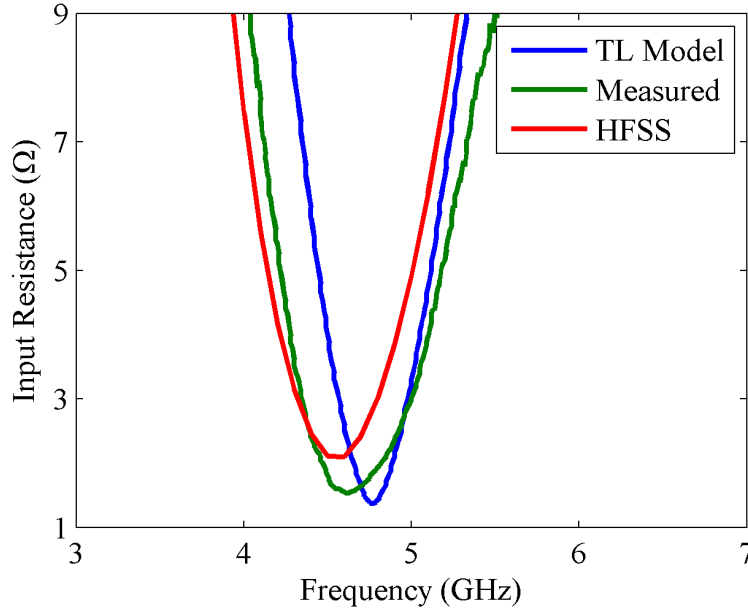


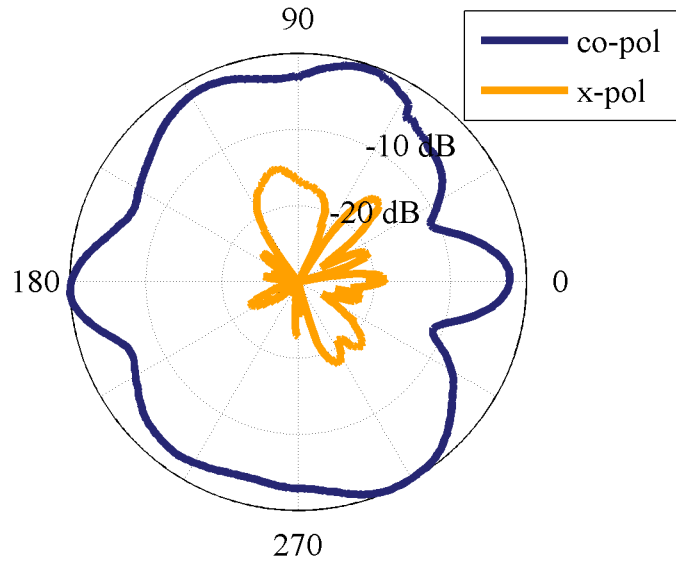
Figure 4.4: VSWR of the slot antenna with the microchannel empty

since the resonant frequency is inversely proportional to channel length. However, the channel length was constructed to be slightly longer, giving a channel resonance at 4.74 GHz, as shown in Figure 3.8.

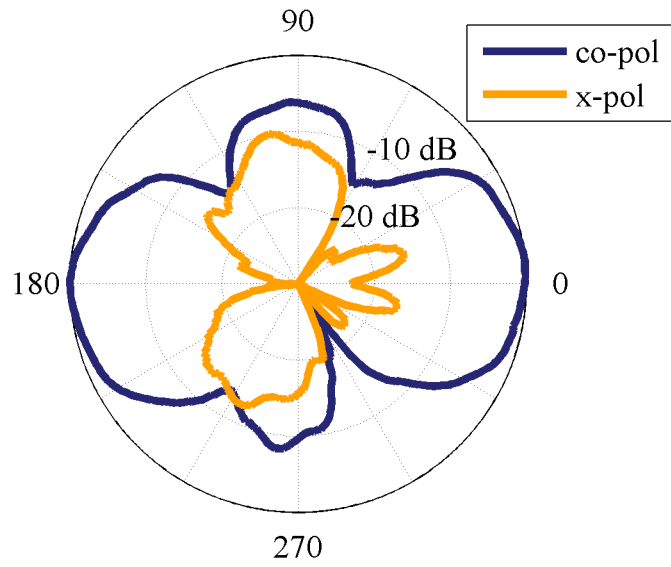
The input impedance of the reconfigured antenna is shown in Figure 4.6. The measured input impedance indicates a resonance at 5.27 GHz. The transmission line model does a good job of modeling the effect of this input impedance shift due to manufacturing tolerances. An additional effect occurs at about 3.8 GHz, where the length of the slot and microchannel combine to be a half wavelength. The transmission line mode at 3.8 GHz is captured by the transmission line model quite well, however.

The VSWR plot in Figure 4.7 indicates a very similar effect for the match, with very good model behavior at the designed frequency. The best match for the measured antenna occurs at 5.34 GHz. The undesired transmission line mode at about 3.8 GHz is matched quite well and will need to be suppressed. The model still gives a narrower bandwidth than the simulated or measured antennas.

The radiation patterns appear in Figure 4.8 at 5.34 GHz with the same definitions as in the previous section. The patterns are still that of a radiating magnetic dipole, indicating that the switch does not significantly affect the radiating mechanism of the slot, allowing the switch to reconfigure frequency

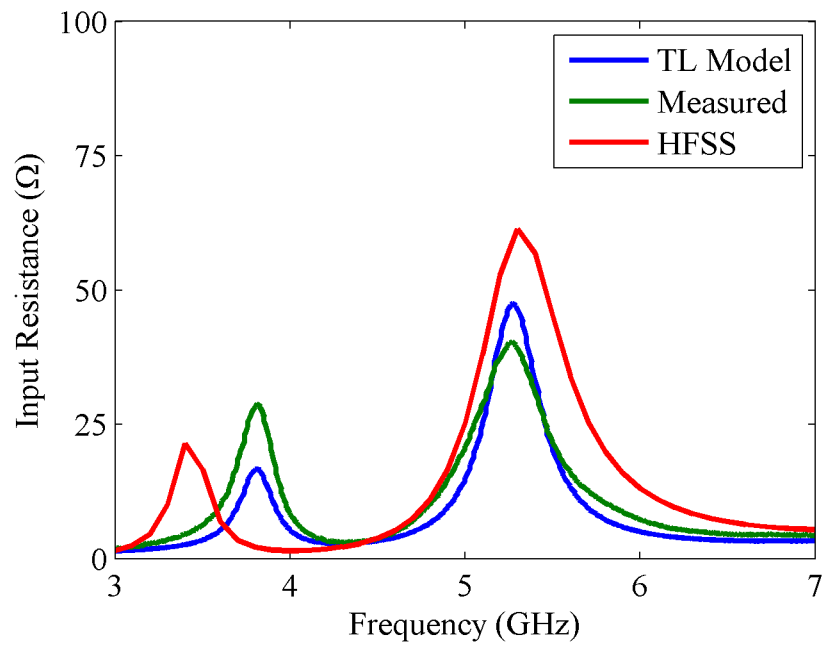


(a) E-plane

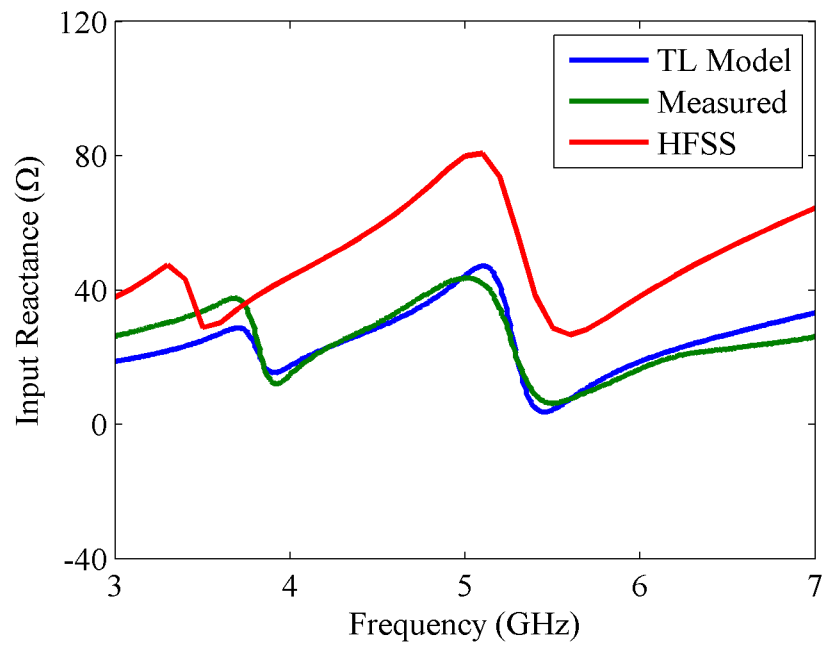


(b) H-plane

Figure 4.5: Radiation patterns of the slot antenna with the microchannel empty at 4.6 GHz



(a)



(b)

Figure 4.6: Input impedance of the slot antenna with the  $\lambda_c/2$  channel filled



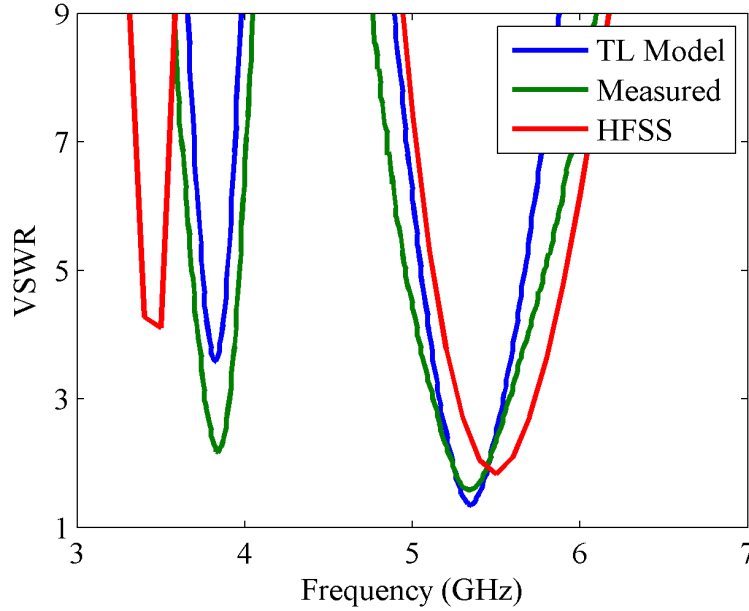
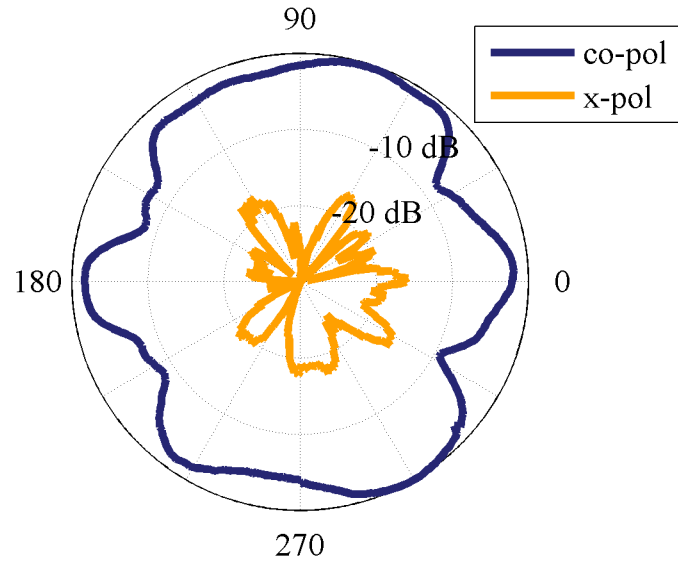


Figure 4.7: VSWR of the slot antenna with the  $\lambda_c/2$  channel filled

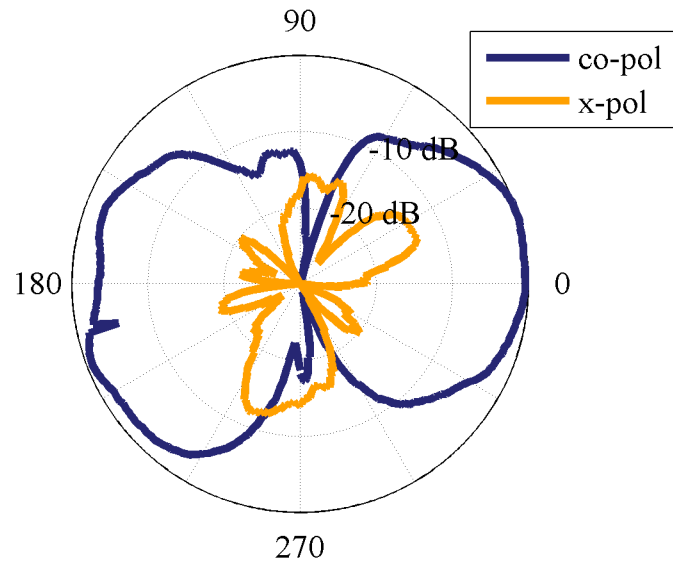
without drastically changing the antenna performance. The lobed behavior, particularly in the H-plane pattern, is diminished because the ground plane is longer in electrical dimensions at this higher frequency, allowing for the currents to diminish more before reaching the edges and radiating.

#### 4.3.1 Effects of Evacuating the Microchannel

A major concern with microfluidic antennas is the possibility of thin films of the fluid remaining in the microchannels and keeping the antenna from being able to effectively be reconfigured back to its original state. To investigate this effect, the microchannel was evacuated using air pressure and then cleaned using an alcohol solution. The antenna was measured again, with the results appearing in Figure 4.9. The input impedance of the antenna, while slightly different than before filling the microchannel, is not changed significantly. This result indicates that this antenna will be able to reconfigure and then return to the original operating conditions. However, the channel evacuation may be improved in the future by exploring ways to reduce residual surface wetting in the channel.



(a) E-plane



(b) H-plane

Figure 4.8: Radiation patterns of the slot antenna with the  $\lambda_c/2$  channel filled at 5.34 GHz

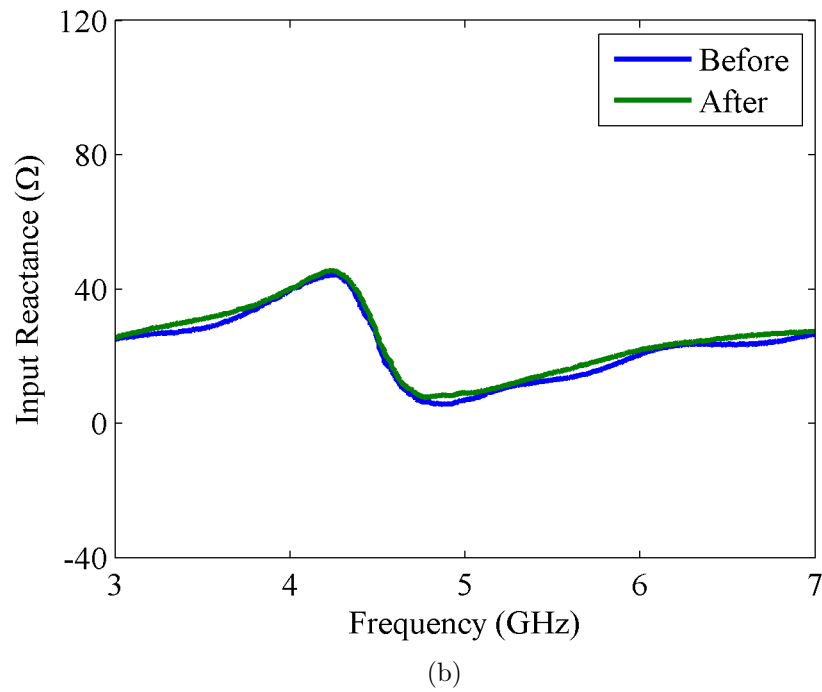
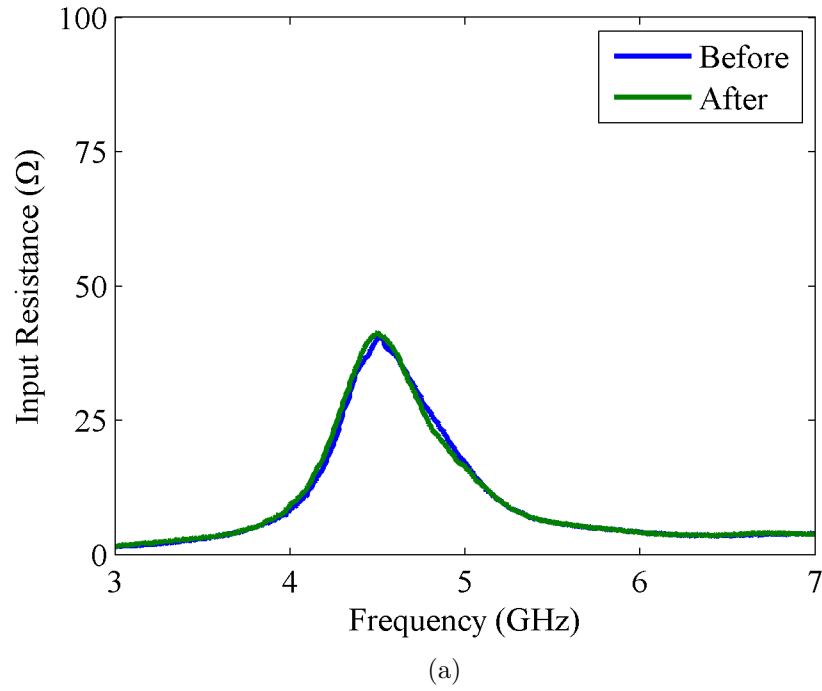


Figure 4.9: Comparison of input impedance of the antenna before the microchannel is filled and after it is evacuated

## 4.4 Long Microchannel Slot Results

### 4.4.1 Empty Microchannels

The second antenna was also modeled and measured, though the long microchannels precluded the possibility of using simulation software due to the small grid size necessary to capture the effects of the microchannels. The input impedance of the antenna with empty microchannels is shown in Figure 4.10. The resonance occurs at 4.68 GHz for both the model and the measured data, with a peak resistance of 95  $\Omega$ . This antenna does not have quite as good a match to 50  $\Omega$  at resonance due to the feed being placed at 2 mm rather than slightly below, as seen in the VSWR plot in Figure 4.11. The best match occurs at 4.94 GHz, away from resonance.

The radiation patterns of the antenna with empty channels are shown in Figure 4.12. The antenna radiates as a magnetic dipole, just as expected, with lobes from the finite ground plane.

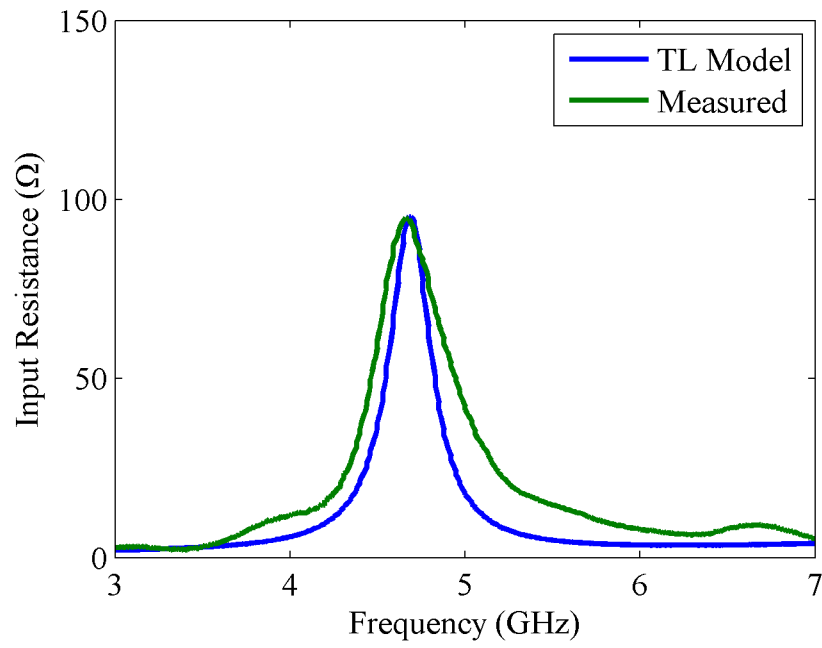
### 4.4.2 Single Microchannel Filled

Filling the first microchannel results in an input impedance shown in Figure 4.13. The long microchannel yields a number of transmission line modes which do not correspond to the resonance of a slot of length 20 mm:

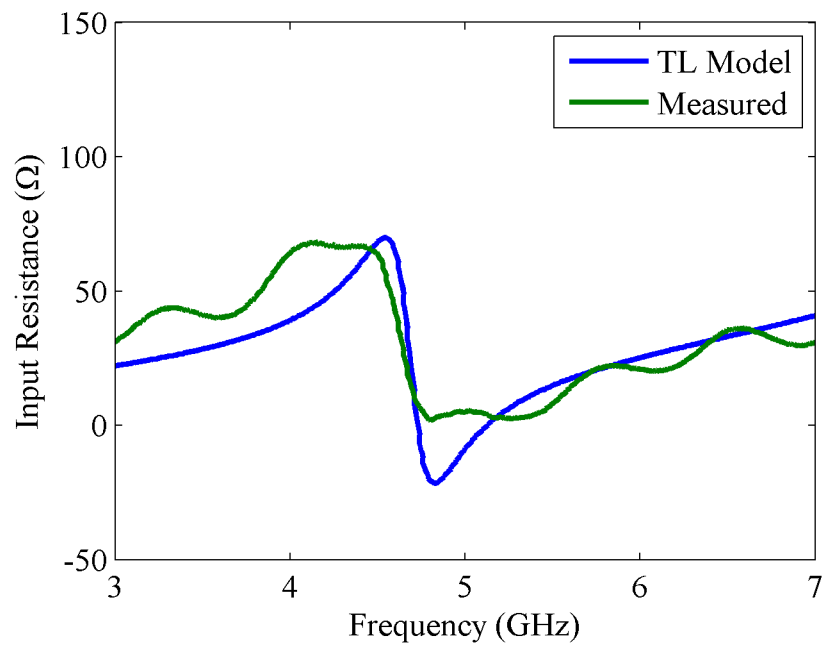
$$f_1 = f_0 \frac{22 \text{ mm}}{20 \text{ mm}} = 5.1 \text{ GHz.} \quad (4.4)$$

The long microchannel cannot be effectively used as a switch for this slot antenna, but the model very accurately predicts the behavior of the microchannel, indicating that it can be used away from the ideal  $\lambda_c/2$  lengths for this work.

The VSWR plot in Figure 4.14 indicates that several modes will be matched, which would allow for this antenna to operate as dual-band if it were designed to do so. However, the radiation patterns in Figure 4.15 indicate that the radiation of the antenna is affected by this switch, as the H-plane radiation pattern does not have any indication of a null in the vertical direction. This is due to the fact that part of the half-wavelength current distribution is not radiating but is residing on the channel, close to the ground plane.



(a)



(b)

Figure 4.10: Input impedance of the second slot antenna with the channels empty

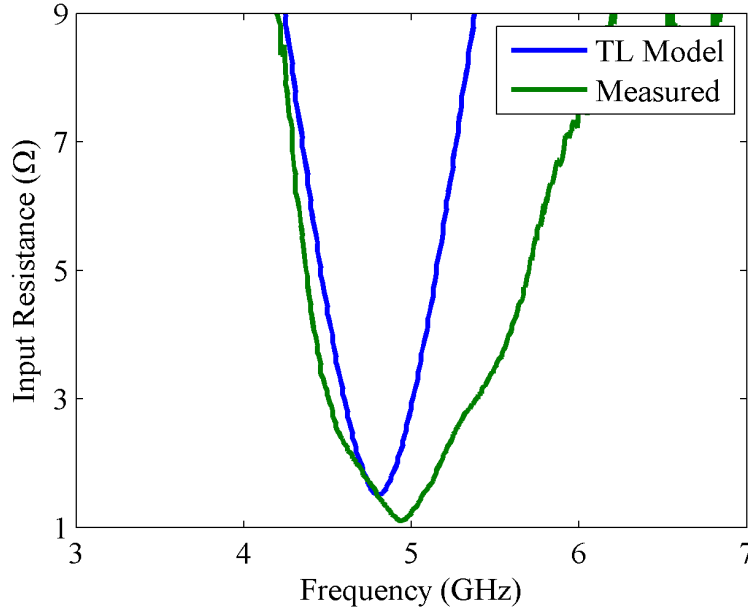


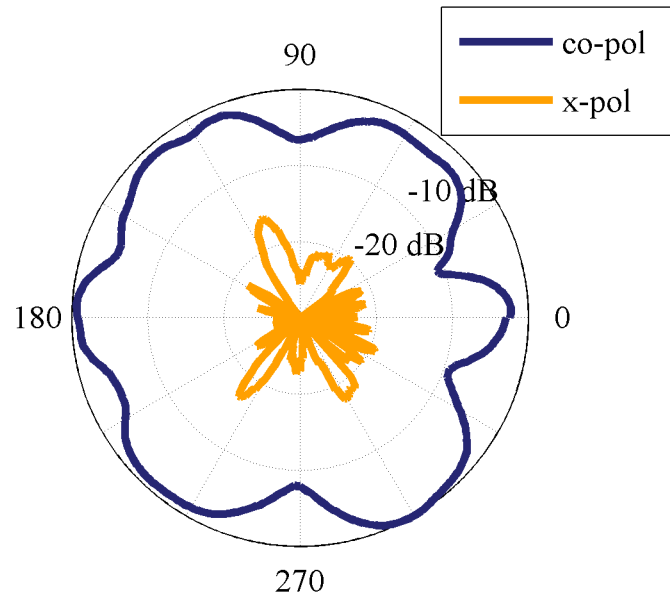
Figure 4.11: VSWR of the second slot antenna with the channels empty

#### 4.4.3 Two Microchannels Filled

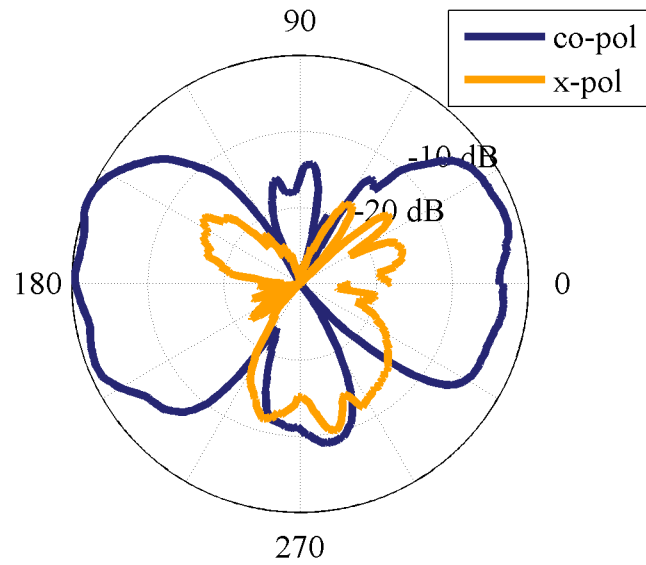
The last case that was evaluated was the antenna performance with two long channels filled in the second antenna. The two long channels will add multiple modes, as seen in the measurement data in Figure 4.16 and Figure 4.17. While the slot model captures some of the modes in the antenna response, one of the modes is not captured at all and the magnitudes of the resistance and reactance are not very close. The model does not take any coupling between channels into account, which is likely the cause of these discrepancies.

### 4.5 Summary

The results show that the conductive fluid switches designed in Section 3.4 successfully reconfigure the resonant frequency of the slot antenna. However, the filled microchannel also introduces transmission line modes which cause the antenna to be matched at frequencies other than the desired frequency of operation. Additionally, the transmission line model is quite accurate for slot antenna with and without the microchannel filled with conductive fluid, even at nonideal channel lengths. In order to understand the behavior of the antenna with multiple channels filled, though, the transmission line

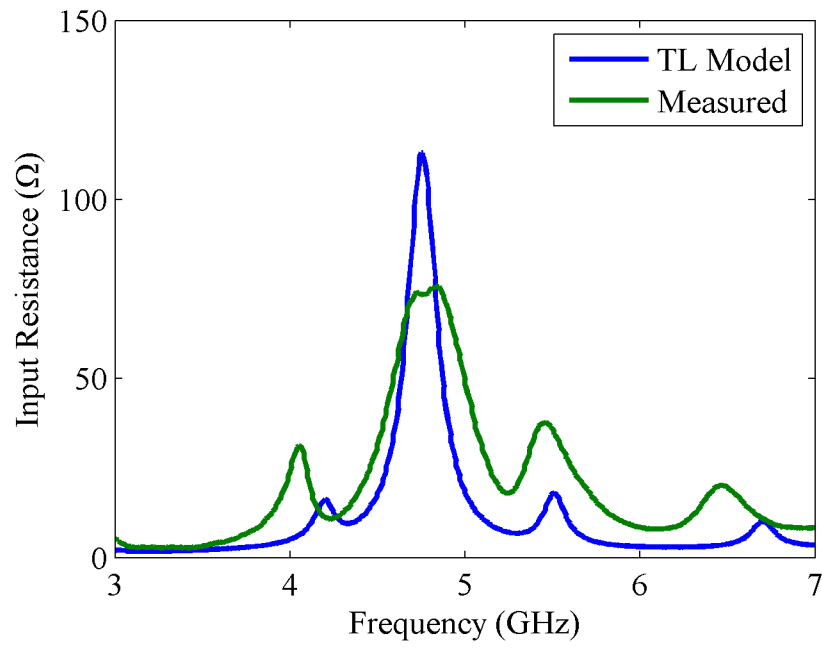


(a) E-plane

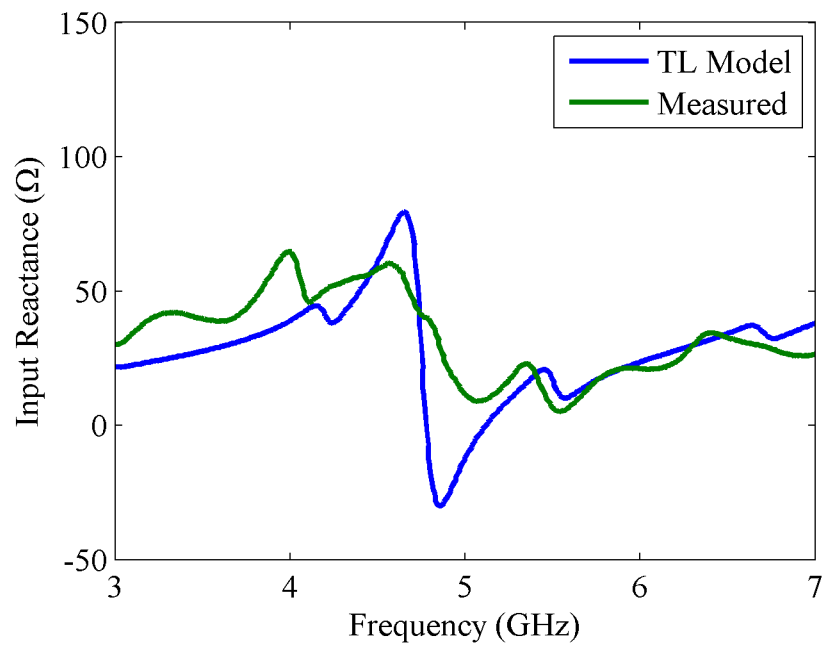


(b) H-plane

Figure 4.12: Radiation patterns of the second slot antenna with the microchannels empty at 4.93 GHz



(a)



(b)

Figure 4.13: Input impedance of the second slot antenna with the first channel filled



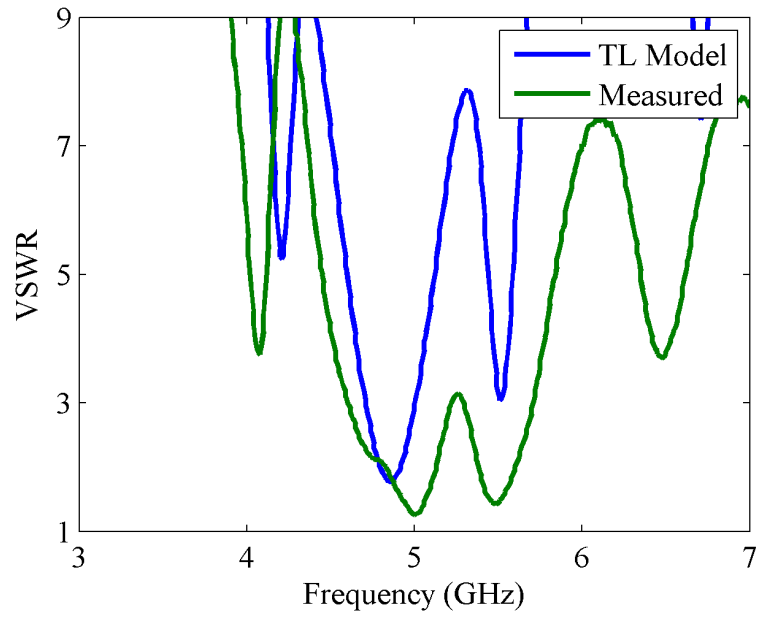
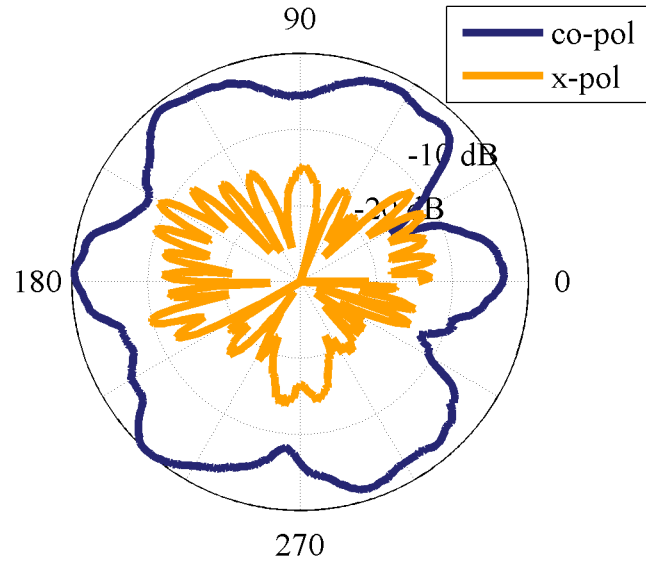
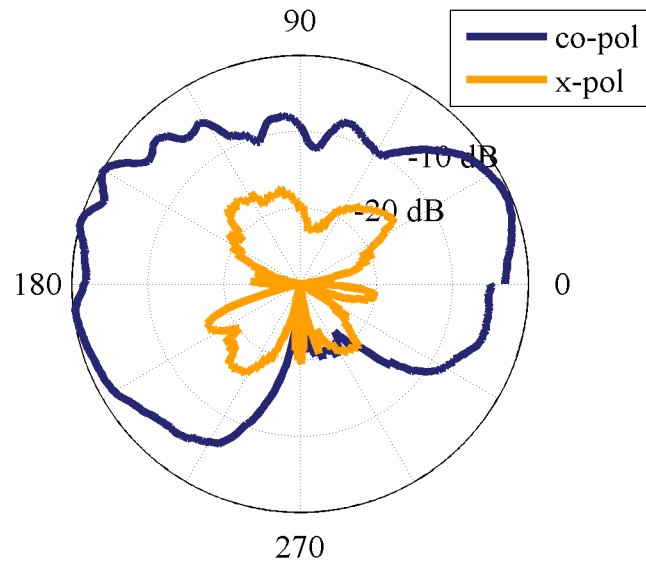


Figure 4.14: VSWR of the second slot antenna with the first channel filled

model needs to be improved to include the coupling behavior between the two closely spaced filled microchannels.

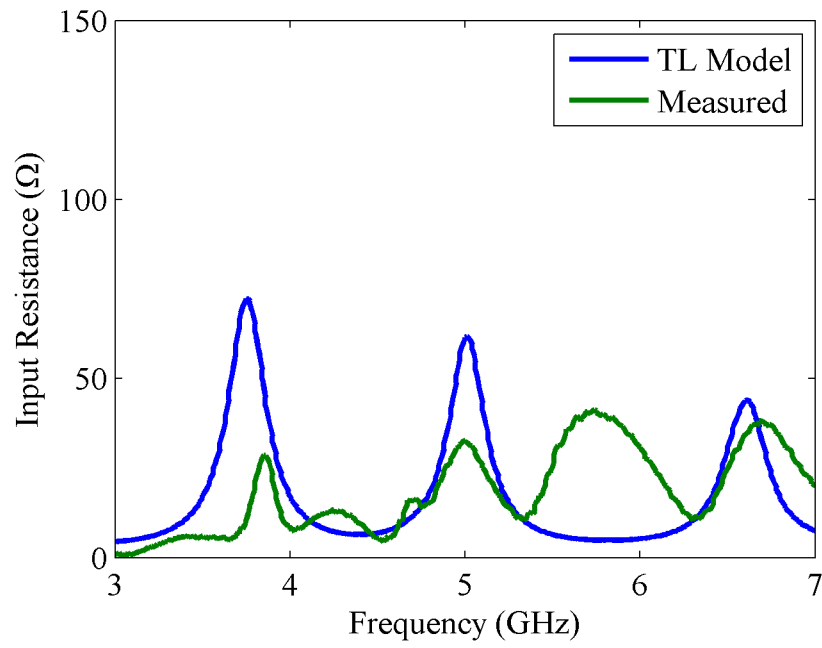


(a) E-plane

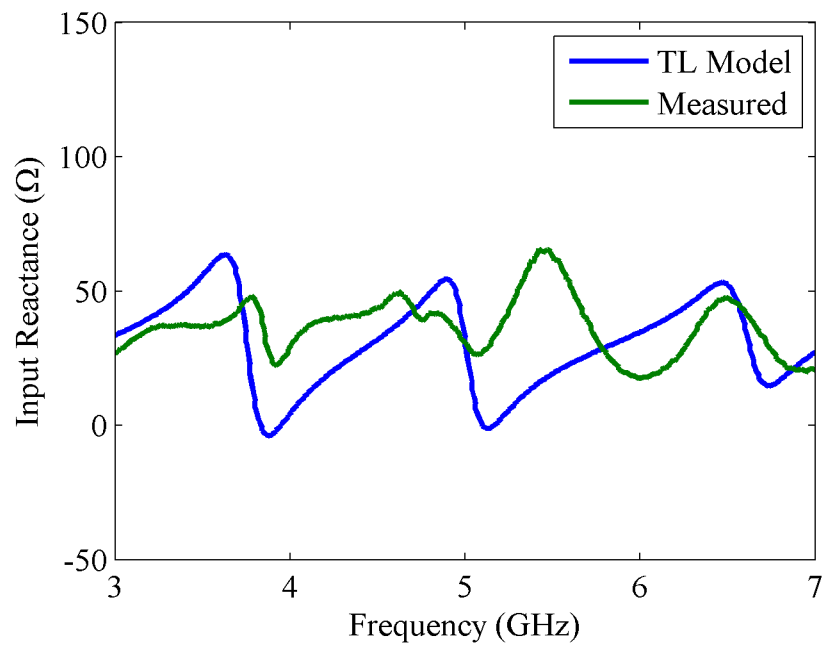


(b) H-plane

Figure 4.15: Radiation patterns of the second slot antenna with the first microchannel filled at 5.5 GHz



(a)



(b)

Figure 4.16: Input impedance of the second slot antenna with two channels filled

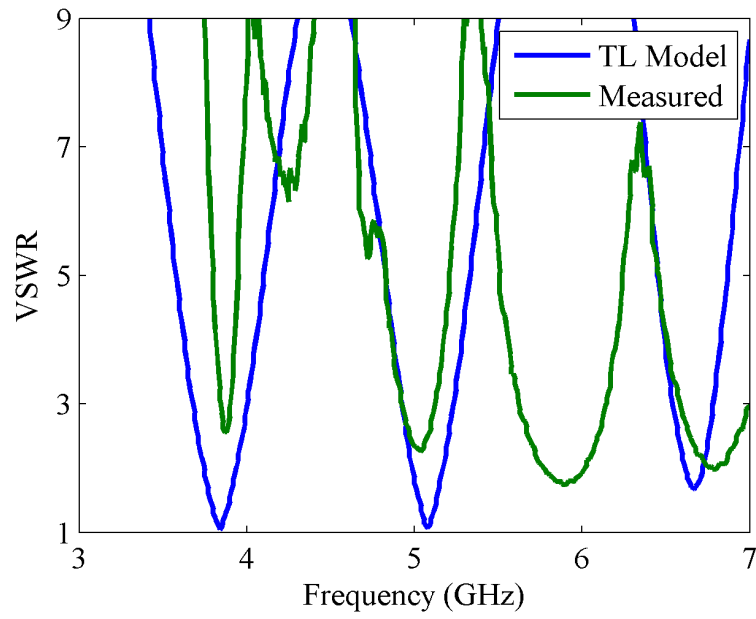


Figure 4.17: VSWR of the second slot antenna with two channels filled

# CHAPTER 5

## CONCLUSIONS AND FUTURE WORK

### 5.1 Conclusions

While reconfigurable antennas have been widely studied, the current state-of-the-art reconfiguration mechanisms do not allow for high power operations. Varactors, PIN diodes, and RF MEMS devices each have issues dealing with high power signals which prohibit certain high power applications from being able to take advantage of the benefits of reconfigurability within the RF system.

The issues that plague the reconfiguration mechanisms currently being used in research do not appear for microfluidic systems, which are passive and likely will not change their behavior in the presence of strong fields. However, microfluidic reconfiguration mechanisms in antennas have not been studied extensively. This work has demonstrated the viability of reconfiguration based on microvascular delivery of conductive fluid. The microfluidic switches can be implemented relatively easily, without having to segment the ground plane of the radiating element, and have predictable behavior.

A transmission line model of the microvascular switches has been developed in order to provide a suitable design process for antennas using microfluidic switches of this kind. The model allows for the design of a reconfigurable slot antenna with an original operating frequency and a discretely switched alternate frequency.

Additionally, the antenna was shown to be able to not only change operating frequency, but also return to the original operating frequency. Previous microfluidic antennas have either required precise positioning during reconfiguration or have not been able to return to original operating conditions, but the antenna in this work can be reconfigured multiple times, offering more promise for microfluidic switches as a reconfiguration mechanism.

A number of high power systems stand to benefit from the microfluidic reconfiguration demonstrated in this work, particularly radar and high power communications. Continued investigation of this method needs to be performed in order to verify its usefulness for these systems, but the research which has been performed so far shows that fluidically reconfigured antenna systems have promise for use in high power reconfigurable RF systems.

## 5.2 Future Work

Three significant areas of future work need to be pursued in order to move this technology toward being implemented in communications or radar systems, including transmission line mode suppression, power handling analysis, and reconfiguration system design.

### 5.2.1 Transmission Line Mode Suppression

The transmission line modes generated by the filled microchannel switches have the potential to interfere with antenna operation by allowing significant reception of unwanted signals. If the modes give an input impedance relatively near  $50\ \Omega$  at a frequency within the operating bandwidth, this antenna loses its advantage of frequency agility without receiving signals in nearby frequency bands.

The most expedient way to suppress these modes is to improve the substrate fabrication process so that the microchannel allows for points which contact the ground plane, allowing for a physical short to be built across the slot. This method does not rely on transmission line behavior and will therefore not have the undesired modes. Additionally, this method will decrease the amount of coupling that can occur between multiple microchannels, as there are not extended lengths of transmission line coupling to each other.

### 5.2.2 Power Handling Analysis

The primary motivation for this switch type is to provide reconfigurability for high power systems. While current methods clearly cannot handle high

power, and this method does not have the issues associated with these systems, the actual power handling capabilities of microfluidic switches have not been studied. Three issues which still need to be explored are the energy dissipated as heat in the antenna, the dielectric breakdown of the substrate, and the current crowding limitations from the small microchannel. Additionally, the antenna performance while transmitting high power signals needs to be measured to ensure that no other issues need to be addressed.

### 5.2.3 Reconfiguration System Design

The bias networks used for the electrical reconfiguration devices are replaced in this case with a pumping mechanism which will need to effectively inject and evacuate galinstan from the channel. In order to complete the validation of this reconfiguration mechanism as a viable high power switching solution, the pumping system needs to be designed and demonstrated in order to understand the size requirements and speed limitations imposed by such a system. The system also needs to be designed so that the antenna is not significantly affected by the presence of the pump or any other components required for reconfiguration. The completion of this system along with its characterization will allow for a full understanding of the abilities and limitations of microfluidic switching mechanisms for use in reconfigurable antenna design.

## REFERENCES

- [1] J. T. Bernhard, *Reconfigurable Antennas*. San Francisco, CA: Morgan & Claypool, 2007.
- [2] S. Yong and J. Bernhard, "Design of a pattern null reconfigurable antenna," in *2010 IEEE International Symposium on Phased Array Systems and Technology (ARRAY)*, Oct. 2010, pp. 376–380.
- [3] J. Ruyle, "Small, dual band, placement insensitive antennas," Ph.D. dissertation, Univ. of Illinois, Urbana, Dec. 2011.
- [4] H. Booker, "Slot aerials and their relation to complementary wire aerials (Babinet's principle)," *Journal of the Institution of Electrical Engineers - Part IIIA: Radiolocation*, vol. 93, no. 4, pp. 620–626, 1946.
- [5] D. Peroulis, K. Sarabandi, and L. Katehi, "A planar VHF reconfigurable slot antenna," in *IEEE Antennas and Propagation Society International Symposium, 2001*, vol. 1, 2001, pp. 154–157.
- [6] Y. Chen, X. Liu, Y. Jiao, and F. Zhang, "A frequency reconfigurable slot antenna," in *2007 International Symposium on Microwave, Antenna, Propagation and EMC Technologies for Wireless Communications*, Aug. 2007, pp. 516–518.
- [7] E. Erdil, K. Topalli, M. Unlu, I. Istanbuluoglu, E. U. Temocin, H. I. Atasoy, O. Bayraktar, O. A. Civi, S. Demir, S. Koc, and T. Akin, "Reconfigurable slot antenna with fixed-fixed beam type RF MEMS capacitors," in *Proceedings of the First European Conference on Antennas and Propagation (EUCAP)*, Nov. 2006, pp. 1–5.
- [8] N. Behdad and K. Sarabandi, "A varactor-tuned dual-band slot antenna," *IEEE Transactions on Antennas and Propagation*, vol. 54, no. 2, pp. 401–408, Feb. 2006.
- [9] C. White and G. Rebeiz, "Single- and dual-polarized tunable slot-ring antennas," *IEEE Transactions on Antennas and Propagation*, vol. 57, no. 1, pp. 19–26, Jan. 2009.



- [10] C.-Y. Chiu and R. Murch, "Reconfigurable slot antenna using switched stub technique," in *IEEE International Workshop on Antenna Technology, 2009*, Mar. 2009, pp. 1–4.
- [11] Y. Li, Z. Zhang, W. Chen, and Z. Feng, "Polarization reconfigurable slot antenna with a novel compact CPW-to-slotline transition for WLAN application," *IEEE Antennas and Wireless Propagation Letters*, vol. 9, pp. 252–255, 2010.
- [12] A. Ramadan, M. Al-Husseini, K. Kabalan, A. El-Hajj, and C. Christodoulou, "A polarization reconfigurable slot antenna," in *Proceedings of the 5th European Conference on Antennas and Propagation (EUCAP)*, Apr. 2011, pp. 402–404.
- [13] M. Fries, M. Grani, and R. Vahldieck, "A reconfigurable slot antenna with switchable polarization," *IEEE Microwave and Wireless Components Letters*, vol. 13, no. 11, pp. 490–492, Nov. 2003.
- [14] M. Sonkki, M. Berg, J. Pihlaja, S. Karhu, H. Jantunin, and E. Salonen, "Varactor tunable helical antenna," in *Proceedings of the Second European Conference on Antennas and Propagation (EUCAP)*, Nov. 2007, pp. 1–6.
- [15] S. Lim, C. Caloz, and T. Itoh, "Metamaterial-based electronically controlled transmission-line structure as a novel leaky-wave antenna with tunable radiation angle and beamwidth," *IEEE Transactions on Microwave Theory and Techniques*, vol. 52, no. 12, pp. 2678–2690, Dec. 2004.
- [16] S. Yong, "Design and analysis of pattern null reconfigurable antennas," Ph.D. dissertation, Univ. of Illinois, Urbana, Jan. 2012.
- [17] L. Dussopt and G. Rebeiz, "Intermodulation distortion and power handling in RF MEMS switches, varactors, and tunable filters," *IEEE Transactions on Microwave Theory and Techniques*, vol. 51, no. 4, pp. 1247–1256, Apr. 2003.
- [18] D. Peroulis, S. Pacheco, and L. Katehi, "RF MEMS switches with enhanced power-handling capabilities," *IEEE Transactions on Microwave Theory and Techniques*, vol. 52, no. 1, pp. 59–68, Jan. 2004.
- [19] I. Reines and G. Rebeiz, "A robust high power-handling (>10W) RF MEMS switched capacitor," in *2011 IEEE 24th International Conference on Micro Electro Mechanical Systems (MEMS)*, Jan. 2011, pp. 764–767.

- [20] C. Panagamuwa, A. Chauraya, and J. Vardaxoglou, "Frequency and beam reconfigurable antenna using photoconducting switches," *IEEE Transactions on Antennas and Propagation*, vol. 54, no. 2, pp. 449–454, Feb. 2006.
- [21] J. Bernhard, E. Kiely, and G. Washington, "A smart mechanically actuated two-layer electromagnetically coupled microstrip antenna with variable frequency, bandwidth, and antenna gain," *IEEE Transactions on Antennas and Propagation*, vol. 49, no. 4, pp. 597–601, Apr. 2001.
- [22] J.-H. So, J. Thelen, A. Qusba, G. J. Hayes, G. Lazzi, and M. D. Dickey, "Reversibly deformable and mechanically tunable fluidic antennas," *Advanced Materials*, vol. 19, pp. 3632–3637, Nov. 2009.
- [23] M. Kubo, X. Li, C. Kim, M. Hashimoto, B. J. Wiley, D. Ham, and G. M. Whitesides, "Stretchable microfluidic radiofrequency antennas," *Advanced Materials*, vol. 22, pp. 2749–2752, Apr. 2010.
- [24] S. Mazlouman, X. J. Jiang, A. Mahanfar, C. Menon, and R. Vaughan, "A reconfigurable patch antenna using liquid metal embedded in a silicone substrate," *IEEE Transactions on Antennas and Propagation*, vol. 59, no. 12, pp. 4406–4412, Dec. 2011.
- [25] M. Rashed Khan, G. J. Hayes, J.-H. So, G. Lazzi, and M. D. Dickey, "A frequency shifting liquid metal antenna with pressure responsiveness," *Applied Physics Letters*, vol. 99, no. 1, pp. 1–3, July 2011.
- [26] G. Huff, D. Rolando, P. Walters, and J. McDonald, "A frequency reconfigurable dielectric resonator antenna using colloidal dispersions," *IEEE Antennas and Wireless Propagation Letters*, vol. 9, pp. 288–290, 2010.
- [27] A. P. Esser-Kahn, P. R. Thakre, H. Dong, J. F. Patrick, V. K. Vlasko-Vlasov, N. R. Sottos, J. S. Moore, and S. R. White, "Three-dimensional microvascular fiber-reinforced composites," *Advanced Materials*, vol. 23, pp. 3654–3658, Aug. 2011.
- [28] S. B. Cohn, "Slot line on a dielectric substrate," *IEEE Transactions on Microwave Theory and Techniques*, vol. 17, no. 10, pp. 768–778, Oct. 1969.
- [29] M. Himdi and J. Daniel, "Analysis of printed linear slot antenna using lossy transmission line model," *Electronics Letters*, vol. 28, no. 6, pp. 598–601, Mar. 1992.
- [30] J. Dyson, "The equiangular spiral antenna," *IRE Transactions on Antennas and Propagation*, vol. 7, no. 2, pp. 181–187, Apr. 1959.

- [31] D. M. Pozar, *Microwave Engineering*. Hoboken, NJ: John Wiley & Sons, Inc., 2005.
- [32] J. Knorr, “Slot-line transitions,” *IEEE Transactions on Microwave Theory and Techniques*, vol. 22, no. 5, pp. 548–554, May 1974.
- [33] N. Das, “Generalized multiport reciprocity analysis of surface-to-surface transitions between multiple printed transmission lines,” *IEEE Transactions on Microwave Theory and Techniques*, vol. 41, no. 6, pp. 1164–1177, June 1993.
- [34] Ansys, “High frequency structure simulator,” Canonsburg, PA, ver. 13.